










Article

# European Radiometry Buoy and Infrastructure (EURYBIA): A Contribution to the Design of the European Copernicus Infrastructure for Ocean Colour System Vicarious Calibration

Gian Luigi Liberti <sup>1,2,\*</sup>, Davide D'Alimonte <sup>3</sup>, Alcide di Sarra <sup>4</sup>, Constant Mazeran <sup>5</sup>, Kenneth Voss <sup>6</sup>, Mark Yarbrough <sup>7</sup>, Roberto Bozzano <sup>8</sup>, Luigi Cavaleri <sup>1,2</sup>, Simone Colella <sup>1,2</sup>, Claudia Cesarini <sup>1,2</sup>, Tamito Kajiyama <sup>3</sup>, Daniela Meloni <sup>4</sup>, Angela Pomaro <sup>1,2</sup>, Gianluca Volpe <sup>1,2</sup>, Chunxue Yang <sup>1,2</sup>, Francis Zagolski <sup>5</sup> and Rosalia Santoleri <sup>1,2</sup>

- <sup>1</sup> Consiglio Nazionale delle Ricerche, Istituto di Scienze Marine (CNR-ISMAR), 00133 Rome, Italy; luigi.cavaleri@ismar.cnr.it (L.C.); simone.colella@cnr.it (S.C.); claudia.cesarini@artov.ismar.cnr.it (C.C.); angela.pomaro@ve.ismar.cnr.it (A.P.); gianluca.volpe@cnr.it (G.V.); chunxue.yang@artov.ismar.cnr.it (C.Y.); rosalia.santoleri@cnr.it (R.S.)
  - <sup>2</sup> Consiglio Nazionale delle Ricerche, Istituto di Scienze Marine (CNR-ISMAR), 30122 Venice, Italy
  - <sup>3</sup> Aequora, 1600-774 Lisbon, Portugal; davide.dalimonte@gmail.com (D.D.); tamito.kajiyama@gmail.com (T.K.)
  - <sup>4</sup> Agenzia Nazionale per le Nuove Tecnologie, l'Energia e lo Sviluppo Economico Sostenibile (ENEA), 00123 Rome, Italy; alcide.disarra@enea.it (A.d.S.); daniela.meloni@enea.it (D.M.)
  - <sup>5</sup> SOLVO, 06600 Antibes, France; constantmazeran@solvo.fr (C.M.); franciszagolski@solvo.fr (F.Z.)
  - <sup>6</sup> Physics Department, University of Miami, Miami, FL 33143, USA; kvoss@miami.edu
  - <sup>7</sup> San Jose State University Research Foundation, Moss Landing Marine Laboratories, MOBY Project, Honolulu, HI 96817, USA; yarbrough@mlml.calstate.edu
  - <sup>8</sup> Consiglio Nazionale delle Ricerche, Istituto per lo studio degli impatti Antropici e Sostenibilità in ambiente marino (CNR-IAS), 16149 Genoa, Italy; roberto.bozzano@cnr.it
- \* Correspondence: gianluigi.liberti@cnr.it; Tel.: +39-6-4993-4281

Received: 28 February 2020; Accepted: 2 April 2020; Published: 7 April 2020



**Abstract:** In the context of the Copernicus Program, EUMETSAT prioritizes the creation of an ocean color infrastructure for system vicarious calibration (OC-SVC). This work aims to reply to this need by proposing the European Radiometry Buoy and Infrastructure (EURYBIA). EURYBIA is designed as an autonomous European infrastructure operating within the Marine Optical Network (MarONet) established by University of Miami (Miami, FL, USA) based on the Marine Optical Buoy (MOBY) experience and NASA support. MarONet addresses SVC requirements in different sites, consistently and in a traceable way. The selected EURYBIA installation is close to the Lampedusa Island in the central Mediterranean Sea. This area is widely studied and hosts an Atmospheric and Oceanographic Observatory for long-term climate monitoring. The EURYBIA field segment comprises off-shore and on-shore infrastructures to manage the observation system and perform routine sensors calibrations. The ground segment includes the telemetry center for data communication and the processing center to compute data products and uncertainty budgets. The study shows that the overall uncertainty of EURYBIA SVC gains computed for the Sentinel-3 OLCI mission under EUMETSAT protocols is of about 0.05% in the blue-green wavelengths after a decade of measurements, similar to that of the reference site in Hawaii and in compliance with requirements for climate studies.

**Keywords:** ocean colour; system vicarious calibration; fiducial reference measurement; Lampedusa; Copernicus; MOBY; MarONet; radiometry; research infrastructure; uncertainty budget

## 1. Introduction

The European Copernicus Program for Earth monitoring (<http://www.copernicus.eu/>) aims to deliver remote sensing capabilities, field measurements, and data processing services that provide users with reliable and up-to-date information related to environmental, climate, and security issues. As part of the Copernicus space component, the European Commission is developing, operating, and planning a series of Sentinel missions for the next 15 years, together with ESA and EUMETSAT. Among these missions, the Sentinel-3 Ocean and Land Colour Instrument (S3 OLCI) is a key component for monitoring the biogeochemical status of the ocean. OLCI is a primary source of ocean color (OC) data for the Copernicus Marine Environment Monitoring Service (CMEMS). For instance, OLCI data are operationally used to advance our understanding of living marine environments and assimilated in the CMEMS models to forecast the evolution of marine ecosystems, together with the other OC third party missions. The Sentinel-2 mission, although mainly developed for land applications, already demonstrates a great potential for coastal applications like sediment and chlorophyll retrieval (e.g., reference [1]), and it is expected to become an operational complement of the CMEMS next phases. OC is also an important dataset for Copernicus Climate Change Service (C3S) to monitor the impact of climate change on marine ecosystems and the ocean carbon cycle [2].

OC science is making an increasing contribution to Ocean Observing systems thanks to continuous global monitoring of biogeochemical variables, to the point that OC missions have become fundamental to the success of the Copernicus Marine and Climate services. This has also raised expectations on the quality of data products. The current threshold requirement for calibration uncertainty of Copernicus satellite OC sensors is 0.5% in the blue-green spectral region, with a further goal of 0.3% [3–5]. OC System Vicarious Calibration (SVC) [4,6] complements pre-launch and on-board calibrations through highly accurate in-situ measurements of water-leaving radiances. These measurements are indeed the principal source for the vicarious calibration of space-born radiometric data. By reducing residual biases in water-leaving radiances, SVC is currently the only way to attain the target OC product uncertainties [7], satisfy OC mission requirements [8], and enable marine and climate data services.

Presently, OC-SVC relies on two sites—the Marine Optical BuoY (MOBY; <https://www.mlml.calstate.edu/moby/>) [9] and the BOUée pour l’acquiSition d’une Série Optique à Long termE (BOUSSOLE; <http://www.obs-vlfr.fr/Boussole/>) [10]—established in the last two decades with different instrumental designs, respectively, in the Pacific Ocean and in the Mediterranean Sea. None of these systems is, however, fully compliant with the operational requirements of the Copernicus Programme. The creation of an OC-SVC infrastructure dedicated to the Copernicus Programme is a key point to improve the performance of OC missions that meet the long-term and high-quality standards underpinning marine bio-geochemistry data products delivered by Climate and Marine Services [5]. EUMETSAT has identified a series of steps to achieve this goal. The first step accomplished in 2017 defined the requirements for the Copernicus OC-SVC Infrastructure [3]. These requirements represent the baseline for the present second step: preliminary design of the Copernicus OC-SVC Infrastructure. The overall objective of this paper is to contribute to this European effort by designing the OC-SVC infrastructure able to provide highly accurate, state-of-the-art Fiducial Reference Measurements (FRM) in the very tight development schedule (36 months from the start development) requested by Copernicus Programme. Our design is to commit to the highest radiometry standards and fast operational readiness. This work will then contribute to the third step: technical definition, specifications, and engineering design that are expected to start in 2020.

The main objective of this paper is to describe the proposed European Radiometry Buoy and Infrastructure (EURYBIA), named for the goddess of power over and mastery of the sea (Εὐρυβία: wide-force; who presided over external forces that influence the main such as the rise of the constellations, seasonal weather, and the power of the winds; Theoi Greek Mythology, [www.theoi.com.](http://www.theoi.com/)) for SVC of current and future Copernicus missions (Sentinel-3 A, B, C, D, Sentinel-2 C, D), as well as of third party missions (e.g., NOAA/VIIRS, NASA/PACE). The paper will demonstrate that the proposed OC-SVC Infrastructure (Figure 1) meets these requirements in terms of core optical system and field

deployment structure hosting it, data processing, and delivery. The deployment site selection will be justified on the basis of environmental conditions, logistic factors, and a complete estimate of the uncertainty budget of the products for the proposed OC-SVC infrastructure.

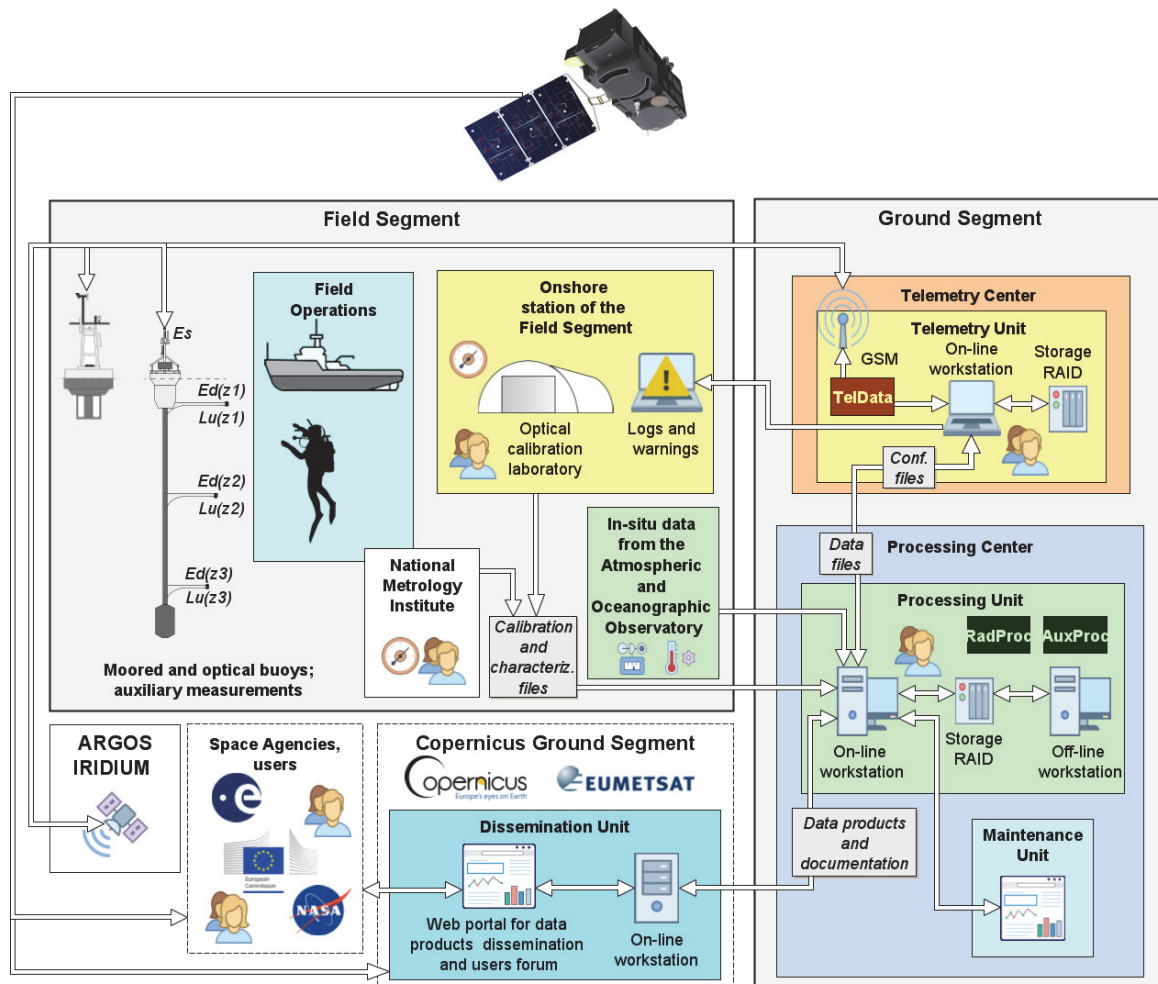


**Figure 1.** The overall concept of the European Radiometry Buoy and Infrastructure (EURYBIA), with the field segment (left) and ground segment (right).

Based on OC-SVC requirements, this paper is structured as follows. Section 2 describes the core EURYBIA optical system, the characterization and calibration procedures, as well as acquisition protocol. The optical buoy and the mooring buoy for the deployment of the optical system and ancillary equipment are presented in Section 3. Solutions featured by the Ground Segment for data telemetry, processing, quality control, dissemination, and the scheduling of maintenance operations are discussed in Section 4. Regarding the location of the site, previous studies [4,11–13] investigated the suitability of a set of candidate regions using, as reference metrics, the number of valid match-ups resulting from a set of single threshold criteria applied to a restricted set of variables. With respect to the previous studies, the OC-SCV requirements [3] encompass a larger number of variables and corresponding constraints taken into account by this paper. This environment assessment includes oceanographic and atmospheric properties and adjacency effect of the proposed selected sites and is summarized in Section 5. Section 6 summarizes the suitability of the site by developing a model to estimate the uncertainty on the vicarious calibration gains and by applying it to OLCI observations [14] and to the results of the characterization study. Final conclusions are addressed in Section 7.

## 2. The Optical System

This section provides a summary of the proposed optical system (2.1) and its characterization and calibration procedures (2.2). Additional information can be found in the existing literature and technical documents [15–18].

### 2.1. Optical System Description

The core instrumentation of EURYBIA is the optical system of the Marine Optical Network (MarONet), developed by the MOBY team on the basis of the long-term experience acquired in the last three decades. In order to fulfil spectral range and resolution requirements, the system actually consists of a common optical path from the radiation collectors to a device that directs the measured signals into two similar single spectrographs covering different spectral regions and named, on the basis of the range the “Blue” (BSG: 350–690 nm) and the “Red” (RSG: 550–900 nm). Figure 2 shows a scheme of the optical system.

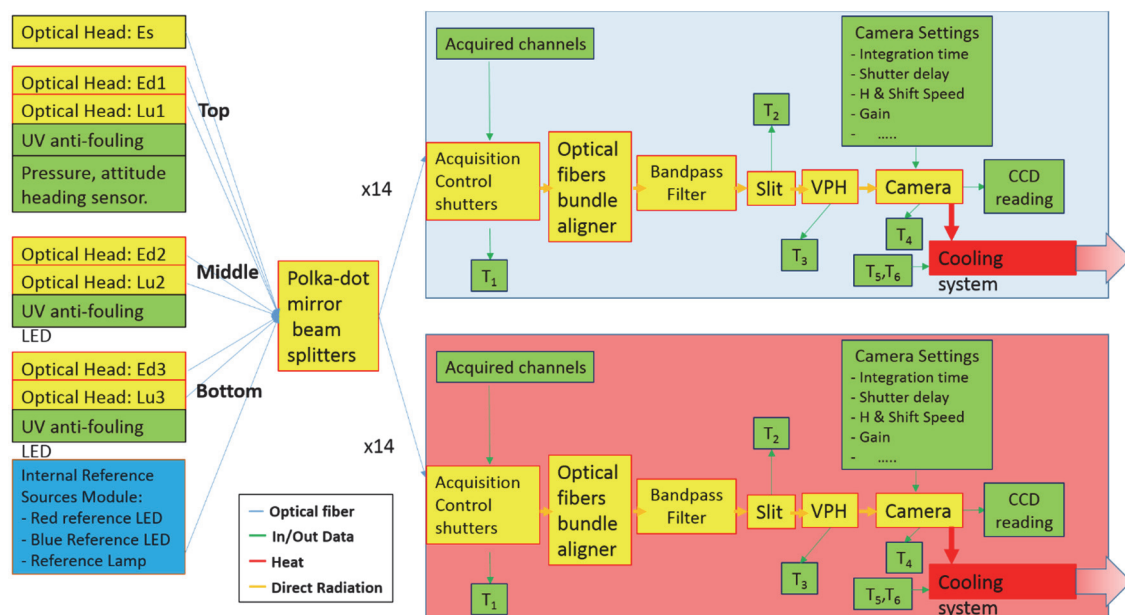


Figure 2. Scheme of the optical system.

The optical signal is collected by the optical heads deployed into the water at the end of each of the three arms (upwelling radiance and downward irradiance measurements, Lu and Ed, respectively) and on the top of the mast of the Optical Buoy (above-water irradiance measurement, Es) (see Section 3). The structure of the optical head depends on the radiometric variable (radiance vs. irradiance) to be acquired, as detailed by Zibordi et al. [12]. To mitigate bio-fouling effects on the optical windows, they are surrounded by a copper bezel and equipped with a UV anti-biofouling module consisting of a fiber optic coupled source of sterilizing UV light (285 nm). The exposure scheme will be programmable to be optimized for the actual site characteristics.

Optical fibers transfer the radiation from each collector to the bottom of the buoy where the two spectrometers are mounted. The signal is split with a polka-dot mirror and transmitted to the two spectrometers. In the following, we describe a single spectrometer. The optical fibers from each collector are connected to a shutter block consisting of 14 single shutters that can also host neutral density filters to adjust the signal level. These devices are also connected, by means of optical fibers, the reference lamps for system monitoring during deployment. Each shutter can be activated independently, allowing the sensor to be illuminated with all possible combinations of inputs.

Optical fibers are aligned on the entrance slit of the spectrometer to allow for the projection on the spectral dispersion system. The alignment order is determined to minimize stray light between different inputs. Band pass filters and short and long wave cutoff filters are mounted at the entrance of the spectral dispersion system to reduce the effects of radiation outside the respective spectral range of the BSG or SRG spectrometer.

The spectral dispersion system is a transmission Volume Phase Holographic spectrograph (VPH) distributed by Resonon Inc., Bozeman, MT 59715, USA. The VPH reduces the stray light by more than one order of magnitude with respect to the concave reflective gratings adopted in MOBY Heritage [19]. The VPH allows imaging all the environmental optical inputs at once: downwelling sky irradiance ( $E_s$ ), downwelling irradiance measurements from the three arms ( $Ed_{Top}$ ,  $Ed_{Mid}$ , and  $Ed_{Bot}$ ), and upwelling irradiance from the three arms ( $Lu_{Top}$ ,  $Lu_{Mid}$ , and  $Lu_{Bot}$ ).

The radiation sensor consists of a scientific Andor Ikon M934 camera, Oxford, UK. The camera is a back illuminated Charged Coupled Device (CCD) with a thicker active photosensitive area (i.e., deep depletion CCD) and fringe suppression to prevent etalon effects. The camera is retrofitted with wedged windows to minimize straylight effect (UV ghosting). Different base settings allow the definition of data acquisition characteristics and the sensor working temperature to optimize the camera performances. System synchronization capabilities are used to control the integrated C-mount shutter that is closed during readout to avoid vertical smear. The system is thermo-electrically cooled to reduce the dark current. For MarONet, the cooling temperature has been set to  $-60\text{ }^\circ\text{C}$  as trade-off between noise reduction, power consumption, long term stability, and lowest drift. Cooling the CCD array provides stability to the camera system eliminating bright and dark pixels while also reducing thermal noise and dark current.

An internal reference system is incorporated into the optical system to monitor the stability of the radiometric detectors, the electronics, and internal optics. These measurements are critical for establishing confidence in the observations acquired during a deployment cycle. The reference system consists of one optical feedback-regulated incandescent lamp and two current regulated, temperature stabilized LEDs. The diodes emit at a wavelength centered at 465 nm (Blue LED) and 705 nm (Red LED), with a bandwidth of approximately 100 nm. The lamps are run with current controlled circuitry and the temperature of the lamp holder block is monitored. Each source output is channeled through a one-inch Spectralon sphere to split between the RSG and BSG. The diffuser is illuminated in sequence by the incandescent lamp, the blue LED, and the red LED. These lamps are observed at the end of each data acquisition set. The internal reference sources give no information on changes of optical properties of the single collectors (for example due to bio-fouling) since these components are not included in the optical path of the reference lamps signals.

The system is designed to allow for fully (also remotely) programmable measurement protocols. This functionality, which can be done remotely, will be exploited mostly in the implementation phase to optimize the characteristics of the measurement protocol scenarios needed for SVC. Table 1 summarizes the characteristics of the proposed optical system and compares them against the corresponding requirements.

A set of additional sensors are associated with the optical system to:

- monitor the status of the system: e.g., temperature of different sub-components, power supply, coolant flow, etc.;
- provide ancillary/auxiliary variables for data processing and/or data quality assessment: e.g., sea water temperature and salinity, top arm depth sensor, tilt along two horizontal axes, system heading.

## 2.2. System Characterization and Calibration

The main objectives of the system characterization are to



- allow the identification of interactions and dependencies between optical and electronic components;
- identify, evaluate, and correct any systematic disturbances;
- allow the design of the Level-0 to Level-1 data processing, estimate input variables, and verify the radiometric model (see Section 4);
- allow the estimate of the contribution of each component to the uncertainty budget associated with the radiometric measurement (see Section 6).

**Table 1.** Compliancy table of the proposed optical system with respect to the ocean color infrastructure for system vicarious calibration (OC-SVC) requirements [3]. T = Threshold, G = Goal.

Item	OC-SVC Requirement	MarONet Specs
Spectral Coverage	380–900 nm (T) 340–900 nm (G)	350–900 nm (B: 350–690 nm + R: 550–900 nm)
Spectral resolution	3 nm (T) 1 nm (G)	0.8–1 nm (FWHM)
Spectral sampling	<1 nm	0.6–0.9 nm
Spectral calibration	0.2 nm	0.01–0.02 nm
Stray light	<i>Characterization Monitoring Correction</i>	Spectral straylight < 5 orders of magnitude over the central signal. Cross track stray light negligible
Radiometric Calibration	1–2% (in air and in the VIS domain)	0.514% @410 nm
Radiometric Stability	1% (during deployment)	1%/deployment
Radiance detector Angular Response	<10° half angle FOV	1.73° full-angle FOV
Immersion Factor	<i>must be measured</i>	Estimated associated ( $k = 1$ ) uncertainty $\approx 0.05\%$ Temperature dependence is obtained from characterization in thermal bath. Operationally, temperature of different system subcomponents is monitored continuously by means of a set of currently 6 (max 14) sensors.
Temperature Dependence	<i>shall be determined continuously</i>	Acquisition protocol includes dark signal acquisition mode before and after each collector/reference lamps signal acquisition.
Dark Signal	<i>shall be measured and corrected</i>	
Polarization Sensitivity	<1%	<0.2%
Linearity	<i>Shall be characterized Instrument noise shall be kept at levels that do not impact the total uncertainty of a measurement.</i>	>99% (but not significant in the measurement range)
Noise Level		CCD readout noise $\sim 2.9$ electrons $\rightarrow < 2$ ADU $\rightarrow \sim 0.003\%$ at full scale

This is achieved through a set of activities consisting of

- full system characterization after complete assembling;
- in-field monitoring;
- post-deployment characterization in case of identified anomaly.

A detailed description of the characterization activities carried out in the period 2014–2018 can be found in Voss et al. (2018) [15]. The complete system characterization should be done for each new unit when the optical system is built and fully integrated. Leaving the details of the characterization to dedicated existing or future literature, we list the following relevant issues that are planned for the system characterization:

- CCD tracks binning factor;

- full images (saturation checks);
- behavior of dark counts;
- integration time correction factor (shutter delay);
- linearity with optical flux (double aperture; variable radiance source);
- temperature sensitivity (water bath);
- wavelength calibration—atomic line emission sources (pre/post), Fraunhofer lines (field);
- spectral and cross track stray light;
- cosine response (Es);
- polarization sensitivity;
- immersion factors.

In addition to the complete system-level characterization when fully integrated, extensive partial characterizations are planned to be performed pre- and post-deployment (see Section 3). The aspects that need to be periodically characterized will depend on the results of the pre-operational phase to be carried out after the infrastructure deployment. For this purpose, a set of tests that can monitor the status of the system can be introduced in the measurement protocol and/or data processing.

The objective of the radiometric calibration is to obtain absolute values of radiometric measurements compliant with the International System of Units (SI) and directly traceable to National Metrology Institute (NMI) primary standards. This is obtained by absolutely calibrating each system before and after optical buoy deployment and by monitoring the radiometric calibration during each deployment [18].

### 3. EURYBIA Field Segment

Based on the MarONet system design [5], the EURYBIA Infrastructure consists of a twin buoy system: an optical buoy tethered to a mooring buoy anchored to the sea bottom (Figure 3). The first buoy carries the optical system to perform the radiometric measurements, whereas the second buoy hosts additional scientific meteorological and oceanographic instrumentation and collects ancillary data.

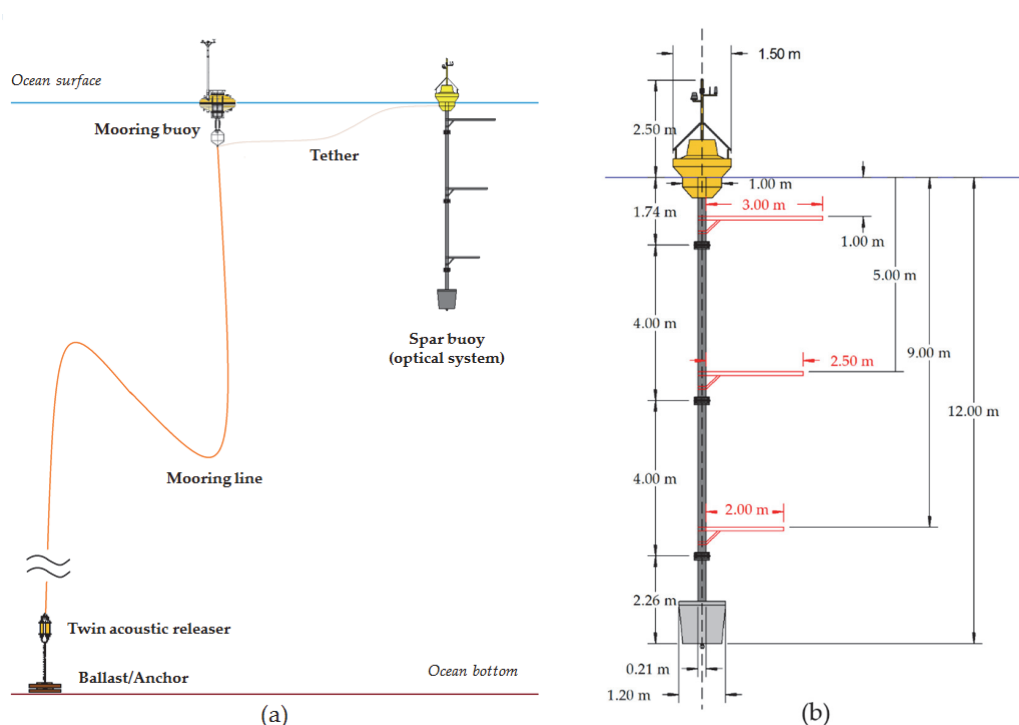


**Figure 3.** (a) Sketch (not to scale) of the main components of the EURYBIA deployment infrastructure; (b) scheme of the optical buoy.

Indeed, collecting measurements useful for OC-SVC implies strict constraints on the motion of the buoy that, on one hand, must follow the wavy surface to keep each optical collector at a constant depth and, on the other, must maintain tilting oscillations to within a few degrees in order not to bias the optical measurements.

In order to guarantee the operational measurements, we propose to design and build two identical infrastructures in order to enable rotation in the field, always having one system operational at sea and the other ashore for maintenance operations to make it ready for the next deployment. This design allows the system to be compliant with the critical requirements of the measurement traceability achievable only with frequent periodic on-site and on-land maintenance and calibration operations while ensuring the continuity of the long-term observations.

### 3.1. Optical Buoy

The optical buoy, hosting the radiometric system, consists of a medium-size spar buoy [9] whose actual dimensions, distribution of masses along the structure, and tether connection to the mooring buoy are properly designed to optimize the buoy stability due to local environmental conditions (i.e., reduced tilting with respect to the sea state conditions) and self-shading effects. Figure 3 shows a preliminary scheme of the optical buoy; the reported dimensions and depths of the three arms hosting the in-water optical collectors are based on MarONet design. The final design, optimized to the environmental conditions of the selected site, might require minor adjustments. Indeed, a spar buoy is characterized by a reduced section at the water surface, a deep draft, a long vertical hull, a disk on the deepest level, and a ballast. These characteristics, relevant to reduce heave (i.e., the buoy vertical motion) and tilting also allow the deployment of instruments along the long vertical hull. For the EURYBIA application, the buoy is also designed to follow the surface in order to keep the optical instruments at constant depths with respect to the sea surface, which is achieved by ensuring a substantial capacity of floating reaction.

The structure of the optical buoy can be divided into the following main parts, each one contributing to the overall structure buoyancy while housing instruments and electronic components essential for the system operational activity: a top floatation element, a hull, and a lower bay.

The top floatation element hosts a payload consisting of an Es irradiance cosine collector, antennas for the positioning and communication system, a radar reflector, a lantern, photovoltaic panels and batteries to power up all electronic systems, an industrial controller collecting data and operating the whole system through A/D converters and/or serial channels, a modem for the communication system, and controllers.

Along the hull, at different fixed depths, three arms support the in-water optical collectors—one for downwelling irradiance and one for upwelling radiance. The arms have different lengths, the longer being closest to the surface and the shorter at the deepest position in order to avoid any interference on upwelling radiance measurements. On the shallower arm, a pressure sensor is also installed in order to monitor the depth of the upper arm measurement.

Two industrial data loggers, connected through an Ethernet connection, are deployed on the optical spar buoy: one data logger collects the optical measurements, located underwater in the watertight lower bay, and a second data logger, which is installed in the watertight compartment on the main floatation element, collects all other data and monitoring parameters (i.e., orientation of the arms, temperatures inside the watertight compartment, depth of the shallower arm, trim of the buoy, current produced by the photovoltaic panels, voltage of the batteries, etc.). At the bottom of the buoy, an orientation module consisting of a pressure sensor and an attitude and heading reference system are installed in order to monitor the trim of the collector and to provide information for any compensation of the acquired irradiance. All data acquired on board are packed into a data cluster, timestamped, and geographically annotated by the upper controller, locally stored on the hard disk while constituting the stream of bytes to be transferred ashore with a communication (telemetry) system.



All the above-mentioned electronic systems and sensors are powered by the photovoltaic panels and batteries installed on the infrastructure itself, which are self-sustained for the entire period of activity, considering up to four acquisition cycles per day, also including the payload required by the necessary alert and monitoring services.

### 3.2. Mooring Buoy

A mooring buoy consisting in a standard disc-shaped surface buoy is anchored to the sea bottom and is tethered to the spar buoy to keep the optical buoy in place. It also hosts additional equipment to support the radiometric data collection, processing, quality assessment, and results interpretation.

The following parts of the payload of the mooring buoy are similar to the those installed in the optical buoy: antennas for the positioning and communication system, a radar reflector, a lantern, photovoltaic panels and batteries to power all electrical systems, an industrial controller collecting data and operating the whole system through A/D converters and/or serial channels, a modem for the communication, and controllers for the photovoltaic panels.

Additionally, the mooring buoy hosts an attitude and heading reference system to measure the motion of the buoy and instruments for collecting ancillary measurements above the sea surface and underwater. A meteorological station is required to process and interpret the radiometric observations. Optionally, above-water instrumentation may include radiometric measurements with the main objective of estimating the presence of clouds, and in-water standard bio-optical instrumentation could be installed to support main radiometric data processing and quality assessment.

As for the optical buoy, all above-mentioned electronic systems and sensors get their electrical power supply from a system of photovoltaic panels, charge regulators, and batteries.

## 4. Ground Segment

Ground segment (GS) tasks include telemetry operations, processing of the in-situ measurements to derive radiometric products and related uncertainties for the computation of SVC gains, dissemination of results, documentation of processing code, and scheduling of maintenance operations. The telemetry center and the processing center described in the next sub-sections are the two main infrastructural components that allow for GS activities, as detailed hereafter.

### 4.1. The Telemetry Center

The telemetry center executes direct and independent data transfers with the mooring and optical buoy by means of GSM communication. Its specific tasks are (1) uploading configuration files with instrumentation settings and acquisition protocols, (2) uploading firmware programs for the EURYBIA equipment, and software modules for the onboard controllers, (3) executing preliminary data processing and checks, (4) downloading in-situ measurements, and (5) verifying the status of buoys at sea and alerting in the case of out-of-order conditions. This latter assignment relies on a continuous (24/7) acquisition of monitoring parameters, even when radiometric and auxiliary measurements are not collected. Integrity checks are performed to detect transfer errors (checksum), missing values in data records, or out-of-range conditions (e.g., temperature, position and power supply). Redundant communication and storage resources, as well as functionalities to remotely supervise and restart telemetry operations, ensure continuous control of the buoys system at sea. In case of anomalies, including missing communication signal, alerts are immediately released to start recovery actions.

### 4.2. The Processing Centre

In-situ measurements are transferred from the telemetry center to the processing center to compute data products. The data processing is structured in levels to control the complexity of code, simplify its maintenance and evolution, facilitate the assessment of intermediate results, and allow for starting data reprocessing on demand from the specified processing level (Figure 4).

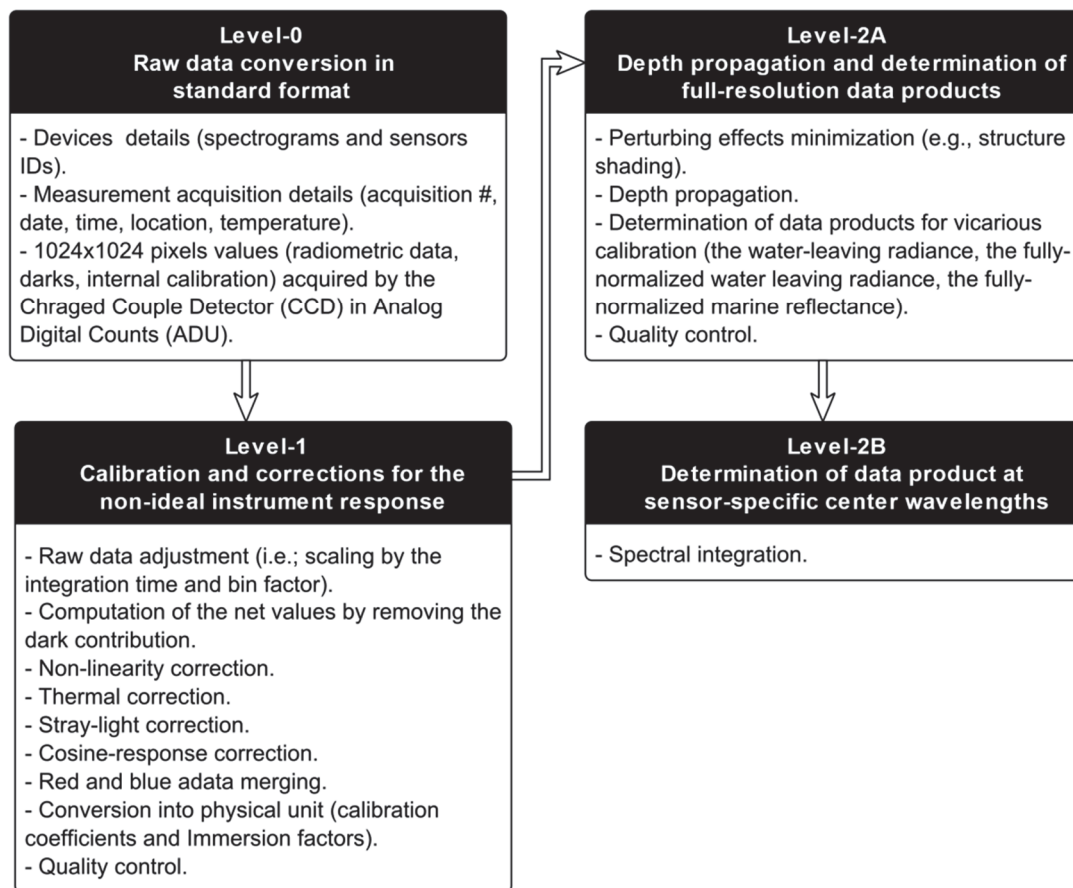


Figure 4. Schematics of processing levels.

The Level-0 processing accounts for the raw data conversion into a standard format. The Level-1 processing applies corrections for the non-ideal instrument response and computes calibrated values in physical units. The Level-2A proceeds to the minimization of environmental perturbations, performs depth propagation of in-water radiometric measurements and computes full-resolution data products such as the water-leaving radiance. The Level-2B finally derives data products at center wavelengths of specific space-borne sensors (spectral integration). Intermediate results and final products are archived as independent output files. Processing settings and metadata for the identification of input measurements and the version of the processing model are also recorded.

#### 4.2.1. Level-0

The format of raw data produced by the radiometric system might change through time due to instrument updates or revisions of the EURYBIA data acquisition program. The Level-0 processing is then scoped to convert raw data into a standard format.

#### 4.2.2. Level-1

Data recorded at the CCD of the Resonon spectrogram are expressed in Analog Digital Units (ADU). The Level-1 processing corrects these input data accounting for the non-ideal radiometer response and generates results in physical units. An additional task is a spectral calibration to relate CCD column-wise pixels to wavelengths.

The formalism adopted in this manuscript is derived from the “Protocols for Satellite Ocean Colour Data Validation: In-situ Optical Radiometry” report of the International Ocean-Colour Coordinating Group (IOCCG) [7]. Denoting with the symbol  $\mathfrak{J}(\lambda)$  either  $L(\lambda)$  or  $E(\lambda)$  in physical units ( $\text{W}\cdot\text{cm}^{-2}\cdot\text{sr}^{-1}\cdot\text{nm}^{-1}$  and  $\text{W}\cdot\text{cm}^{-2}\cdot\text{nm}^{-1}$ , respectively), the Level-1 conversion equation is

$$\mathfrak{I}(\lambda) = F_I(\lambda) \cdot F_C(\lambda) \cdot \mathfrak{N}(\lambda) \cdot \tilde{\mathfrak{I}}(\lambda), \quad (1)$$

where:

1.  $\tilde{\mathfrak{I}}(\lambda)$  represents net radiometric data obtained by subtracting the dark contribution from signal data after scaling the raw CCD readouts by the measurement integration time (sec) and the binning factor (unit of a pixel, pix)— $\tilde{\mathfrak{I}}(\lambda)$  is thus in units of  $\text{ADU} \cdot \text{sec}^{-1} \cdot \text{pix}^{-1}$ , see for instance [20];
2. The term  $\mathfrak{N}(\lambda) = \mathfrak{N}_{\text{NL}}(\lambda, \mathbf{X}_{\text{NL}}) \cdot \mathfrak{N}_{\text{T}}(\lambda, \mathbf{X}_{\text{T}}) \cdot \mathfrak{N}_{\text{SL}}(\lambda, \mathbf{X}_{\text{SL}}) \cdot \mathfrak{N}_{\text{CR}}(\lambda, \mathbf{X}_{\text{CR}})$  accounts for the non-ideal instrument response due to non-linearity (NL) [21], temperature (T) [22], stray-light (SL) [23–25]; non-cosine response (CR) of the above-water irradiance sensor [26–28] (with  $\mathbf{X}$  denoting input parameters for the specific correction; e.g., temperatures for T, sun elevation and tilt for CR, etc.);
3.  $F_C(\lambda)$  indicates the in-air absolute calibration coefficient (i.e., the absolute responsivity) in units of  $(\text{W} \cdot \text{cm}^{-2} \cdot \text{sr}^{-1} \cdot \text{nm}^{-1}) / (\text{ADU} \cdot \text{sec}^{-1} \cdot \text{pix}^{-1})$  and  $(\text{W} \cdot \text{cm}^{-2} \cdot \text{nm}^{-1}) / (\text{ADU} \cdot \text{sec}^{-1} \cdot \text{pix}^{-1})$  for the radiance and irradiance data, respectively;
4.  $F_I(\lambda)$  is the immersion factor accounting for the change in responsivity of the sensor when immersed in water with respect to air (dimensionless).

Results obtained from measurements performed by the blue and red spectrographs are finally merged into a unique spectrum (for each sampling acquisition and radiometric sensor). This processing step requires as input the predefined cut-off wavelength at which the spectra are joined.

#### 4.2.3. Level-2A

The first processing step is the minimization of shading effects due to the deployment structure and the radiometers housing by means of look-up tables (LUTs) produced with Monte Carlo (MC) simulations of the radiative transfer process for given boundary conditions [29–31]. The scheme to determine the shading correction factors executes, for the same environmental case, MC ray tracing with and without accounting for the presence of the optical buoy. The difference between the two results defines the shading correction coefficients [32].

The biofouling effect is evaluated by means of specific quality checks performed during the periodical cleaning of the radiometers. These monitoring results are used to evaluate changes in the instrument performance and compile information to assess the data products quality.

The sub-surface value of the upwelling radiance is derived from  $L_u(z_i, \lambda)$  measurements performed at three fixed depths  $z_i$  ( $i = 1, 2, 3$ ), with  $z_1 > z_2 > z_3$  and assuming positive depth increasing towards the bottom [28,33]. Precisely, the value of the upwelling radiance just below the sea-surface  $L_u(0^-, \lambda)$  is derived from the  $L_u(z_1, \lambda)$  measurement at the shallowest depth  $z_1$  as

$$L_u(0^-, \lambda) = L_u(z_1, \lambda) e^{K_L(0,1, \lambda) \cdot z_1}, \quad (2)$$

where  $K_L(0, 1, \lambda)$  is the attenuation coefficient of the diffuse upwelling radiance for the depths from 0 to  $z_1$ —i.e.,  $K_L^{01}$  [33]. The diffuse attenuation coefficient  $K_L(i, j, \lambda)$  in the depth interval  $[z_i, z_j]$ , is defined as

$$K_L(i, j, \lambda) = -\frac{\ln \left[ \frac{L_u(\lambda, z_j)}{L_u(\lambda, z_i)} \right]}{z_j - z_i}. \quad (3)$$

The value of  $K_L(0, 1, \lambda)$  cannot be directly measured and is determined from  $L_u(z_1, \lambda)$ ,  $L_u(z_2, \lambda)$  and  $L_u(z_3, \lambda)$  values [33]. To this end, the data processing accounts for the increasing fraction of light generated by inelastic radiative processes (Raman effect and chlorophyll fluorescence) from the blue region of the spectrum, where energy is abundant, to the red region, where the incoming light is rapidly attenuated (this implies a  $K_L$  tendency to decrease with depth for  $\lambda > 575$  nm). MC simulations are employed to compute  $K_L$  lookup tables accounting for Raman scattering [33]. The effect of chlorophyll fluorescence is instead estimated from in-situ measurements in the  $[0, z_1]$  interval performed with

ancillary instrumentation of the moored buoy. The  $K_L^{01}$  estimate is finally modelled as a function of the  $K_L^{12}$  and  $K_L^{13}$  [33].

The water-leaving radiance [6,34,35],  $L_w(\theta, \phi, \lambda_j)$ , is computed as

$$L_w(\theta, \phi, \lambda_j) = L_u(0^-, \theta', \phi, \lambda_j) \frac{1 - \rho(\theta', \theta)}{[n(\lambda_j, T, S)]^2}, \quad (4)$$

where  $\phi$  is the azimuth angle,  $\theta$  is the zenith angle in air,  $\theta'$  is the corresponding refracted nadir angle in water,  $\rho(\theta, \theta')$  is the internal Fresnel reflectance, and  $n(\lambda_j, T, S)$  is the refractive index of seawater, with  $T$  and  $S$  indicating the temperature and salinity, respectively [36].

The fully normalized water-leaving radiance,  $L_{wN}(\lambda_i)$ , is the radiance leaving the sea surface from the water body (i.e., excluding the contribution of incident light reflected above the sea surface) as if the sun was at the zenith, the Earth was at its mean distance from the sun and in the absence of any atmospheric loss [37].  $L_{wN}(\lambda_i)$  is determined as

$$L_{wN}(\lambda_i) = C_{f/Q}(\theta_0, \lambda_i, Chla) \cdot F_0(\lambda_j) \cdot \frac{L_w(\lambda_i)}{E_s(\lambda_i)}, \quad (5)$$

where (1)  $E_s(\lambda_i)$  is the incident solar irradiance; (2)  $C_{f/Q}(\theta_0, \lambda_j, Chla)$  is the BRDF correction term obtained from look-up-tables as a function of the solar zenith angle  $\theta_0$ , the wavelength  $\lambda_j$ , and the Chlorophyll-a concentration  $Chla$  [38]; and (3)  $F_0(\lambda_i) = \overline{F_0}(\lambda_i) \cdot \delta_0(SDY)$  is the extraterrestrial solar irradiance  $\overline{F_0}$  corrected for the Earth-sun distance  $\delta_0(SDY)$  indicating with  $SDY$  the Sequential Day of the Year.

The fully normalized marine reflectance,  $\rho_{wN}(\lambda_i)$ , is finally derived from  $L_{wN}(\lambda_i)$  as

$$\rho_{wN}(\lambda_i) = \frac{L_{wN}(\lambda_i)}{F_0(\lambda_i)} \cdot \pi. \quad (6)$$

#### 4.2.4. Level-2B

Full resolution data are determined in the 350–900 nm interval. Spectral integration is addressed to compute radiometric values for the channel identified by the central wavelength  $\lambda_i$  of selected space-borne sensors as

$$L_w(\lambda_i) = \frac{\int L_w(\lambda_j) \cdot SRF_i(\lambda_j) d\lambda_j}{\int SRF_i(\lambda_j) d\lambda_j}, \quad (7)$$

indicating with  $SRF_i$  the spectral response function of the  $i$ -th band of the space-borne sensor. Note that the numerical integral corresponding to Equation (7) is performed after interpolation of SRF discrete values to the central wavelengths of the in-situ measurement. The numerical integration scheme is then designed to minimize the uncertainty budget. Selected ocean color space sensors of interest include

1. Ocean and Land Color Instrument (OLCI); Sentinel 3 missions; Copernicus Program; EU.
2. Moderate Resolution Imaging Spectroradiometer (MODIS); Terra/Aqua; NASA; USA.
3. Visible Infrared Imaging Radiometer Suite (VIIRS); Suomi NPP, NOAA-20, JPSS-2, JPSS-3; NASA/NOAA; USA.
4. Ocean Color Instrument (OCI); Plankton, Aerosol, Cloud, ocean Ecosystem (PACE) program, NASA [39] (<https://pace.gsfc.nasa.gov/>, planned launch in 2022).

#### 4.3. Quality Assurance and Quality Control

The determination of data products is complemented by the quality assurance and control (QA/QC) of results. This task is jointly based on objective parameters (e.g., coefficient of variation of CCD data at

Level-1, stability of pre- and post-deployment calibration coefficients, presence of optical stratifications limiting the capability to perform depth propagation of the upwelling radiance at Level-2), as well as the visual inspection of results (e.g., abnormal presence of spikes in Level-1 data) and complementary information (e.g., cloud-cover conditions). Additional QA/QC is performed checking the consistency of individual records with historical measurements once the time series permits (in analogy to the procedure adopted by the MOBY Team). For a final assessment, the stability of calibration lamps within their life cycle (i.e., determined based on traceability with respect to standards performed by the National Metrology Institute) is also verified.

QA/QC results are finally summarized through the following labels:

- GOOD indicates the highest quality data for SVC applications (reprocessed data only) or for validation and monitoring (these include near-real-time products release);
- QUESTIONABLE refers to data products derived upon applying significant corrections (e.g., excessive sensor tilting or instability of the instrument response); and
- BAD is applied to data that are unreliable and cannot be used even if the current set of correction schemes are applied (usually caused by unanticipated problems during data acquisition or clouds).

#### 4.4. Data Products Dissemination

The data processing cycle accounts for the following three main release versions:

1. Near Real-Time (NRT) results are delivered once the following operations have been executed: visual data inspection, data correction and calibration, computation of data products such as the normalized water-leaving radiance, and preliminary data quality assurance and control (QA/QC). The timely dissemination of high-quality daily data products derived from in-situ measurements is scoped to release measurements results for the routine assessment and monitoring of orbiting OC remote sensing sensors.
2. Post-Deployment Calibration (PDC) results are computed by performing a data re-processing when the optical system has been recovered to shore and re-calibrated. Namely, pre- and post-deployment calibration coefficients are used to account for instruments responsivity change. Any instrument re-characterization for the non-ideal instrument response is also to be taken into consideration.
3. Finally, Traceable to Calibration Standards (TCS) of NMI supporting OC-SVC activities are determined by means of an additional data re-processing at the end of the operational cycle of calibration lamps (which is in the order of 50 working hours). At this stage, in fact, the lamps are sent to NMI for traceability. Data products are then recomputed when reference calibration sources are replaced (note that the source stability is continuously monitored at the calibration facilities to allow for prompt actions in the case of out-of-order variations).

All GS dissemination services are performed within the Copernicus infrastructure and in compliance with the Copernicus principles of offering free, full, and open access to data and processing models. An interactive data browser will be designed to allow end-users to look up field measurements and derived products for specified search conditions and generate a quick statistical summary of the selected data. Deliverables include details on the pre- and post-deployment calibration coefficients, as well as the stability of calibration sources. Additional services are (1) a web service for the documentation of processing modules and (2) a forum for registered users to provide general information, answer questions, and receive comments and suggestions.

#### 4.5. Maintenance Operations

A web interface is finally dedicated to facilitate the maintenance of the ground segment (e.g., software revisions, hardware replacement) and the field segment (e.g., infrastructure turn-over, instrumentation calibration, cleaning, and replacement). Provided on-line services include the scheduling of maintenance operations and the posting of services logs.



## 5. Site Characterization

### 5.1. Location

#### 5.1.1. Geography and Illumination

As discussed in Section 1, the area around the island of Lampedusa, south of the Strait of Sicily, is proposed as the EURYBIA candidate site for the OC-SVC infrastructure. Lampedusa, part of the small Pelagian archipelago, is a small island (about 20 km<sup>2</sup> surface area) in the open Mediterranean Sea, at 35.5° latitude North. About 6000 inhabitants live in Lampedusa and Linosa, the two major islands of the archipelago. The Lampedusa area has been extensively studied with respect to geomorphology, marine and terrestrial ecology, and many environmental parameters. The archipelago is located on the African tectonic plate, at the southern shoulder of a Plio-Quaternary rift zone that shows deep fault-controlled structural depressions oriented along the North-West to South East direction (e.g., the grabens of Pantelleria, Linosa, and Malta). The associated deep depressions, just North of Lampedusa, are more than 1500 m deep and separate the African continental shelf from that of Sicily. The rift zone is characterized by a moderate seismicity, mostly located in the Linosa graben.

Geologically, the island of Lampedusa is formed by Upper Miocene neritic limestones [40]. The island is about 10 km wide, with a tabular morphology and a surface sloping toward the south and south-east. The maximum altitude is about 130 m.

Calculations of the solar illumination and occurrence of sun glint conditions have been carried out. The illumination conditions at Lampedusa and MOBY are similar in summer, while in winter, the available solar energy at Lampedusa is a minimum of 70% of that available at MOBY. Higher solar zenith angles associated with higher latitude at Lampedusa than at MOBY are favorable for minimizing the influence of sun glint conditions.

#### 5.1.2. Existing Infrastructures

Relevant logistical and scientific infrastructures, and several natural protection areas are present in and around Lampedusa (<http://www.ampisolepelagie.it/>). An airport and a primary and a secondary port exist on the island. Regular daily flights and ferry boats connect Lampedusa and Sicily throughout the year.

With respect to scientific infrastructures, Lampedusa hosts a climate observatory (<http://www.lampedusa.enea.it>), which has been operational since 1997 and is composed of an atmospheric observatory (35.52°N, 12.63°E) [41] and an oceanographic observatory (35.49°N, 12.47°E) [42]. A large number of atmospheric and oceanographic parameters are routinely measured at Lampedusa; these data, together with satellite observations and model results, have been used for the characterization of the Lampedusa area for OC-SVC. In addition, they offer relevant and reliable information for the definition of the design requirements of the buoys structure in order to meet the necessary stability for a higher number of quality measurements throughout the year. The Lampedusa Climate Observatory contributes to global measurement networks and to European environmental research infrastructures, such as the Integrated Carbon Observation System (ICOS) and the Aerosol, Clouds, and Trace Gases (ACTRIS). Lampedusa also contributes to the national network of the European Multidisciplinary Seafloor and water-column Observatory (EMSO), research infrastructure, with a number of oceanographic measurements. The operational instruments include sun photometers, also part of the Aerosol Robotic Network (AERONET), a ceilometer, an aerosol and water vapor lidar, radiometers and spectrometers for downwelling and upwelling radiation and atmospheric remote sensing, oceanographic sensors for temperature, salinity, chlorophyll, CDOM, backscattering, and underwater radiation.

As part of the Lampedusa Climate Observatory, instruments and capabilities in radiometers and spectrometers characterization and calibration (see e.g., references [43–45]) are available on site.

Scientific data acquired at the Lampedusa Climate Observatory have been extensively used, and more than 200 international scientific papers referring to these data have been published so far.

Many studies make advantage of these data for inter-comparison, validation, and combined analyses of satellite observations.

### 5.1.3. Bathymetry

Two regions with bottom depth larger than 300 m at 35.5248°N–12.7667°E and 35.7430°N–12.3579°E, LMP1 and LMP2 respectively, have been identified as possible sites for OC-SVC Infrastructure (Figure 5). These two sites are characterized by a negligible impact from fishing activities and ship traffic and are located at a reasonable distance from Lampedusa (less than 20 km), thus enabling technical operations and allowing for timely interventions, while avoiding any possible adjacency effect (see Section 5.4) and possible influence from emissions occurring on the island.

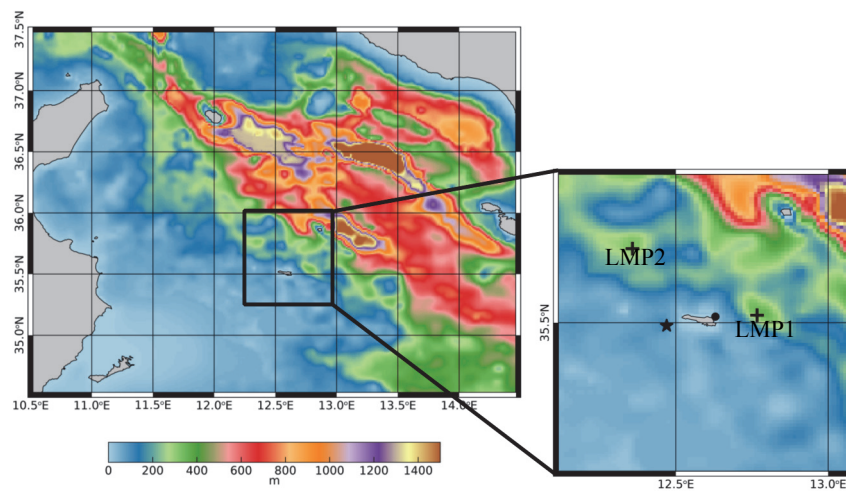


**Figure 5.** Bathymetry of the Sicily Channel with a zoom on the area around the Island of Lampedusa. Black crosses represent possible sites for the future installation (LMP1 and LMP2, respectively, at 35.5248°N–12.7667°E and 35.7430°N–12.3579°E). Black star and filled point show the position of Oceanography and Atmospheric Observatories, respectively.

The bottom effect has been analyzed by performing radiative transfer MC simulations [29,30]. The study acknowledges that the selected region of the Mediterranean Sea is characterized by a relatively high CDOM concentration in comparison with oceanic oligotrophic waters. Light penetration in the water column at the lower end of the spectral region is then significantly limited by the exponential increase of CDOM absorption as wavelength reduces. On the other hand, water absorption lessens the red and near-infrared light transmission. On this basis, 470 nm has been considered as a test wavelength for the bottom effect analysis (specific simulation parameters in Table 2). The bottom contribution has been estimated as percent difference of  $L_u^S$  and  $L_u^B$  values assuming a sandy (S) and a black (B) bottom:

$$\delta_{SB}(z_{btm}) = 100 \cdot \frac{L_u^S(z_{sns}) - L_u^B(z_{sns})}{L_u^B(z_{sns})} \quad (8)$$

where  $z_{btm}$  and  $z_{sns}$  indicate the bottom and the sensor depth, respectively. The value of  $z_{btm}$  has been varied between 50 and 200 m. The value adopted for  $z_{sns}$  is 14 m, which corresponds to the depth of the sensor that is mostly affected by bottom reflectance.

**Table 2.** Parameters employed for the radiative transfer simulations at  $\lambda = 470$  nm.

Sky Radiance			IOPs			Bottom	
$E_s$ [W m <sup>-2</sup> sr <sup>-1</sup> nm <sup>-1</sup> ]	Diff/dir	Sun zenith [deg.]	$a$ [m <sup>-1</sup> ]	$c$ [m <sup>-1</sup> ]	$b_b/b$	Reflectance [%]	Depth [m]
1.57	0.45	15	0.028	0.14	0.0183	0 (B) and 36.2 (S)	50 to 200

The Harrison–Coombes model has been employed for the sky radiance [46,47]. The values of total irradiance and the diffuse-to-direct irradiance ratio have been determined according to [48]. Inherent Optical Properties (IOPs) to model light transfer in the water column have been selected considering the lowest values of absorption, attenuation and backscattering fraction collected in the field [49]. It is highlighted that the minimum measured  $b_b/b$  value is 0.021. However, MC simulations have been executed considering a lower  $b_b/b$  value, namely employing the Volume Scattering Function of Petzold (i.e.,  $b_b/b = 0.0183$ ) [50]. The simulated bottom effect is hence expected to overestimate reality due to larger forward scattering. A Lambertian surface with the reflectance value of coral sand is considered for the bottom [51]. Raman scattering [33] has been neglected because it only accounts for a second-order contribution. Examples of optical profiles for a black and sandy bottom are presented in Figure 6 for water depths of 50 m and 200 m.

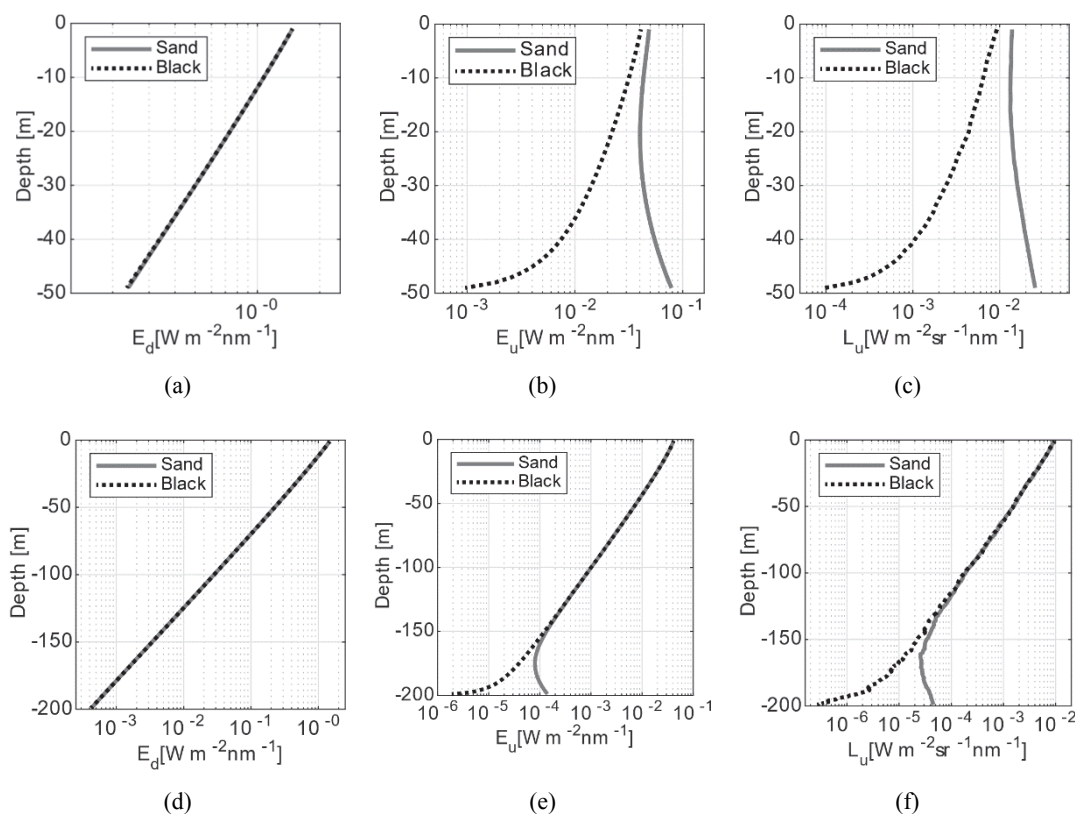


**Figure 6.** Examples of simulation results. (a–f) refer to a bottom depth of 50 and 200 m, respectively.  $E_d$ ,  $E_u$ , and  $L_u$  profiles are from left to right column panels ( $E_d$  and  $E_u$  values presented only for completeness). Simulation results (Table 3 and Figure 7) indicate a negligible contribution to the upwelling radiance at 14 m below the sea surface for a water column of 200 m or deeper.

Results presented in Table 3 and Figure 7 suggest that the impact of bottom reflectance is negligible for a water column of 200 m or deeper, making the selected site with 300 m depth suitable considering the radiometric accuracy required for SVC (i.e., assuming the representativeness of the parameters employed for the MC simulations).

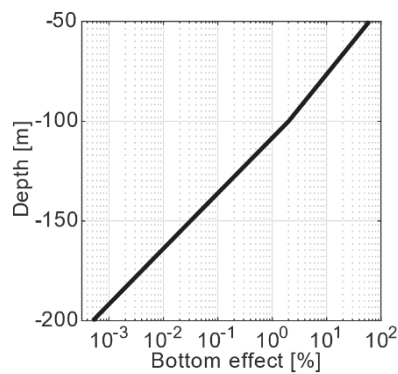


**Figure 7.** Summary of bottom effects simulations (see also Table 3).

**Table 3.** Estimated bottom contribution (percent) to the upwelling radiance at 14 m below the sea surface for different bottom depths.

Bottom Depth [m]	$L_u$ at 14 m Depth [ $W m^{-2} sr^{-1} nm^{-1}$ ]		$\delta$ [%]
	Black Bottom	Sand Bottom	
	Reflectance 0%	Reflectance 39.4%	
−50	$5.289 \times 10^{-3}$	$1.362 \times 10^{-2}$	61.18
−100	$6.911 \times 10^{-3}$	$7.053 \times 10^{-3}$	2.01
−150	$6.005 \times 10^{-3}$	$6.007 \times 10^{-3}$	0.03
−200	$5.895 \times 10^{-3}$	$5.895 \times 10^{-3}$	0.00

## 5.2. Oceanographic Properties

### 5.2.1. Temperature and Salinity

The characterization of the ocean temperature and salinity in the Lampedusa area has been based on in-situ and satellite observations. Data from a conductivity temperature depth (CTD) at 18 m depth, and from a temperature and pressure sensor at a 1 m depth at the Lampedusa Oceanographic Observatory have been used for the reference period 2018–2019. The annual evolution of the temperature and salinity monthly mean values at 18 m depth is shown in Figure 8. By comparison, the range of temperature and salinity at the MOBY site, derived from Feinholz et al. [16], are also shown in Figure 8. The annual temperature cycle is larger at Lampedusa than at MOBY; conversely, the annual salinity changes are significantly smaller at Lampedusa. These variations constitute essential information for the determination of the water refractive index.

Temperature measurements at a 1 m depth show a slightly larger annual cycle than at 18 m, with similar temperatures in winter and somewhat larger temperatures in summer. The temperature daily cycle is generally within  $\pm 3\%$  of the average daily value.

The Sea Surface Temperature (SST) spatial and temporal variability in the region around Lampedusa has been studied based on the daily Level-4 (SST\_MED\_SST\_L4\_NRT\_OBSERVATIONS\_010\_004) product from the Copernicus Marine Environment Monitoring Service (CMEMS) for the reference year 2013. The annual average temperature in the Lampedusa area is about 21 °C. Average day-to-day SST anomalies are generally smaller than 1.5% in the whole area around Lampedusa.

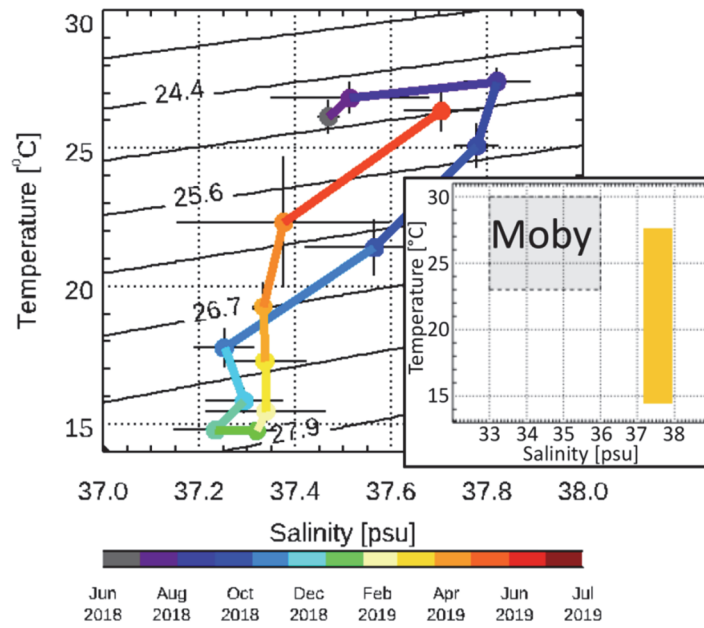


**Figure 8.** Time series of monthly average temperature and salinity, from the 18 m conductivity temperature depth (CTD), at Lampedusa during 2018–2019. The annual range for temperature and salinity at MOBY (grey rectangle) and at Lampedusa (yellow rectangle) is shown in the graph inlet.

5.2.2. Currents

Data for currents at different depths at the proposed sites have been extracted from the CMEMS Med Sea Physical Reanalysis dataset [52]. Daily data for the period 1987–2013 have been used. The information on currents at the Lampedusa area has been compared with current data for the MOBY site retrieved from the CMEMS GLORYS12V1 global reanalysis (<http://resources.marine.copernicus.eu/documents/PUM/CMEMS-GLO-PUM-001-030.pdf>). The reference period that has been considered is 1993–2013.

Figure 9 shows profiles of the median, 99th percentile, and maximum values of currents at LMP1, LMP2, and MOBY. For comparison, also values at the Boussole area (Ligurian Sea), also derived from the CMEMS Med Sea Physical Reanalysis dataset, are displayed.

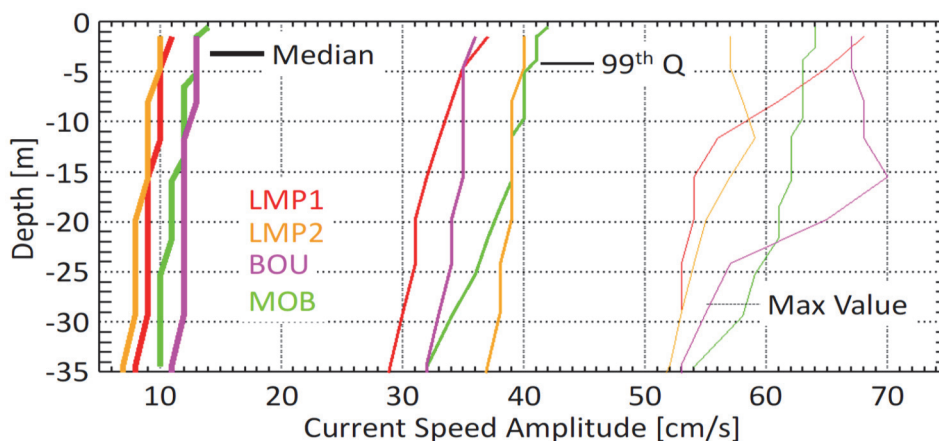


**Figure 9.** Profiles of the median, 99<sup>th</sup> percentile, and maximum values of currents at LMP1, LMP2, and MOBY. For comparison, also values in the Boussole area (Ligurian Sea).

Currents are generally weaker at the Lampedusa area than at MOBY and in the Ligurian sea, although higher current may occur in specific events. All sites show a marked seasonal variability for



the currents, with median smaller values at Lampedusa in all seasons. Dominant currents are from the north-west [53] and are associated with the Atlantic–Tunisian current flowing on the Tunisian shelf.

### 5.2.3. Waves

Data on wave characteristics have been derived from the ECMWF ERA-5 dataset [54]. Data from the period 1979–2019 have been used in the analysis of wave characteristics for both the Lampedusa and MOBY areas. The median of the significant wave height at Lampedusa is about 0.9 m, while it is about 1.1 m in the MOBY area. The significant wave height shows a very limited spatial variability in the region around Lampedusa, much smaller than in the MOBY region. For Lampedusa, the significant wave height is expected to be  $> 1$  m for about 40% of the time. Moreover, relatively high waves are mainly concentrated in winter. Waves from the North-North-West sector are the most frequent, with other smaller contributing sectors from East and South-East.

Significant differences in the wave period exist between the Lampedusa and the MOBY areas. Wave periods are generally shorter at Lampedusa than at MOBY, although a wider range of periods may be found in Lampedusa. The wave characteristics are expected to impact the stability of the buoy attitude; hence, the full wave climate characterization provided with this study aims to offer the backbone of the necessary requirements for the buoys structure design, which is essential for good quality measurements in the long-term.

### 5.2.4. Inherent Optical Properties

The Inherent Optical Properties (IOPs) were investigated using different the CMEMS datasets, for the January 2017–September 2019 period in the Mediterranean, and for the July 2018–November 2019 for the MOBY area; in-situ measurements of chlorophyll, CDOM and backscatter made at the Lampedusa Oceanographic Observatory at 4.5 m depth in the period June 2018–July 2019 [49].

Overall, a very good agreement between satellite and in-situ determinations of chlorophyll is found and confirms that the central Mediterranean is an oligotrophic region. The chlorophyll amount shows a clear annual cycle, with a maximum in winter and a minimum in summer. The annual average chlorophyll amount is  $< 0.08$  mg m<sup>-3</sup> in both the Lampedusa and MOBY regions. The day-to-day variability, as retrieved from satellite observations, is  $< 10\%$  at both sites. The chlorophyll spatial variability is also small ( $< 10\%$ ) in the Lampedusa area. Figure 10 shows the chlorophyll seasonal cumulative distribution as derived from in-situ observations. The chlorophyll amount exceeds 0.2 mg m<sup>-3</sup> only during winter. In-situ continuous observations also show that CDOM and volume backscattering coefficients display an annual cycle, with maxima in winter. Maxima of CDOM and volume backscattering coefficient are 1.1 ppb and  $6 \times 10^{-4}$  m<sup>-1</sup> sr<sup>-1</sup>, respectively. Minima are around 0.5 ppb for CDOM and  $2.5 \times 10^{-4}$  m<sup>-1</sup> sr<sup>-1</sup> for the backscattering coefficient.

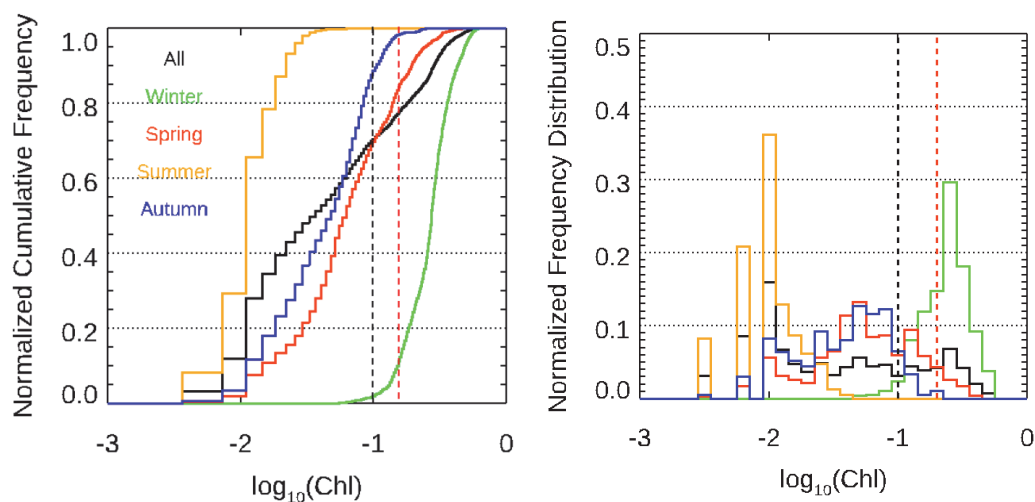


**Figure 10.** Normalized cumulative (left) and frequency (right) distribution of the log<sub>10</sub>-transformed chlorophyll concentration measured at a depth of 4.5 m. Different colors indicate seasons. The black dashed vertical line marks 0.1 mg m<sup>-3</sup>, the red vertical dashed line marks 0.2 mg m<sup>-3</sup>.

### 5.3. Atmospheric Properties

In this section, the main atmospheric properties that may affect SVC are presented and analyzed considering ground-based, satellite, and in-situ measurements.

#### 5.3.1. Meteorology and Local Scale Effects

Because of its reduced surface extension and low and smooth topography, the meteorological conditions at Lampedusa are dominated by synoptic-scale phenomena, while local effects are negligible. Weather patterns display a significant seasonal cycle, with a larger variability during autumn and winter, and generally stable and dry conditions during spring and, particularly, in summer. Precipitation is concentrated in autumn and winter, with a maximum in October. Highest temperatures are registered in August (about 26 °C) and minima in January, February, and March (13.5–14 °C).

The annual cycle in weather variability is also evidenced by tropospheric temperature profiles, showing a temperature inversion from April to August, due to the differential warming of the air and sea surface. From September to March, the absence of temperature inversions is linked to more unstable conditions [55].

The comparison of the temporal evolution of meteorological parameters measured at the atmospheric observatory and at the oceanographic observatory confirms that the island of Lampedusa produces a very small perturbation to the atmospheric dynamics, and local effects are negligible.

#### 5.3.2. Wind

Wind speed is linked to wave formation and with the sea surface roughening and foam, thus limiting the availability of optimal conditions for SVC.

Wind speed patterns are driven by the main synoptic structures, showing prevailing directions from NW, with limited interannual variability. The most frequent wind speed is between 4 m/s and 8 m/s (annual average of about 6 m/s); in about 67% of the cases the wind speed values are <8 m/s (Figure 11).

The wind speed and direction display a seasonal variability, also connected with seasonal changes of the mesoscale Mediterranean atmospheric circulation, with a larger variability during autumn and winter.

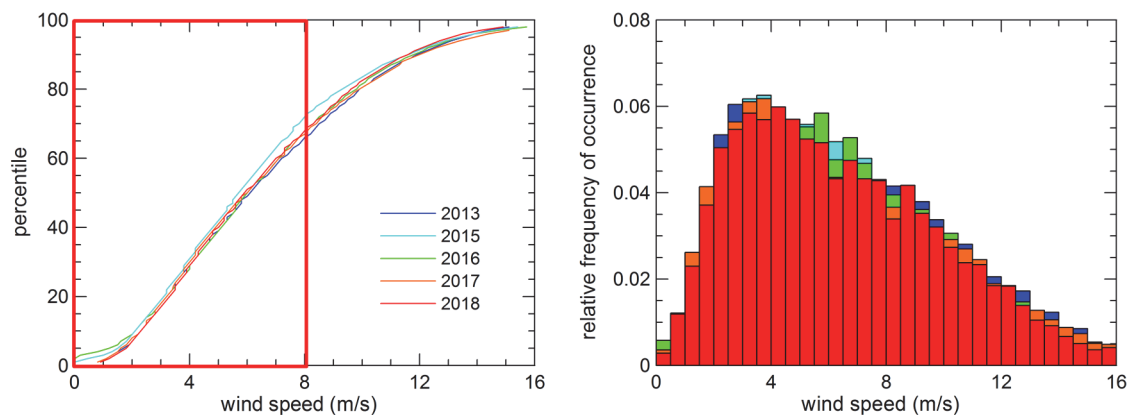


**Figure 11.** Cumulative distribution (**left**) and histogram of relative occurrence (**right**) of the wind speed at Lampedusa. The different curves/histograms are relative to years 2013, 2015, 2016, 2017, and 2018.

### 5.3.3. Cloud Cover

The Sicily channel is an area with relatively low cloud cover occurrence, a moderate seasonal cycle ranging from about 10% in summer to 40% in winter and a relatively low (<5%) interannual variability [56].

The detection of cloud-free periods at Lampedusa is based on ground-based measurements collected by all sky imagers and radiometers. A specific algorithm has been developed to identify cloud-free cases (cloud cover <2 oktas, sun unobstructed) from global and diffuse irradiance measurements made with a Multi Filter Rotating Shadowband Radiometer (MFRSR) [57]. The algorithm is based on the scheme proposed by Long and Ackerman [58], which has been modified to identify periods devoid of clouds also during cases with elevated aerosol amounts, in particular Saharan dust. The method is capable to identify cloud-free cases and has been tested against all-sky imager data. In the paper by [59] (Figure 4 of the cited reference) the frequency of occurrence of cloud-free conditions during the central part of the day (UTC time between 09:00 and 14:00), as derived from 15 years of MFRSR measurements, is shown. Cloud free conditions occur in more than 60% of the cases at Lampedusa during June, July, and August, with peaks of 80%. The frequency is <20% in February, November and December. On average, the area has a 37% overall probability of cloud free occurrence; the interannual variability is relatively low.

Cloud properties retrieved from the MODIS sensor on-board Aqua have been investigated over a region of  $2^\circ \times 2^\circ$  around Lampedusa analyzing Level-3 monthly mean cloud optical thickness, cloud fraction (CF), and cloud top pressure (CTP) from July 2002 to December 2016 (see Figure 10 [59]).

The annual evolution of cloud fraction, with summer minima, is consistent with that of the occurrence of cloud-free conditions. Moreover, covariance of CF and CTP is observed, indicating lowest clouds and smallest CF in July, when low cloud optical thickness values are also observed; this may be associated to the formation of thin low-level cloud at the top of the atmospheric inversion characterizing the marine boundary layer in summer [55]. The spatial distribution of the cloud cover occurrence is highly homogeneous around Lampedusa throughout the year.

Recently, an algorithm to derive cloud cover from measurements of diffuse irradiance at two wavelengths was developed. This algorithm is based on the method developed by Min et al. [60], which uses measurements of diffuse irradiances at 415 nm and 870 nm obtained with an MFRSR instrument. An improved version of the algorithm was implemented, taking into account the effect of aerosol and varying solar zenith angle and leading to an improved determination of cloud cover and to a more general applicability of the method. High time resolution cloud cover was obtained throughout the year 2016 and compared with ground-based sky imager observations, and cloud cover derived from MODIS satellite data. The analysis of those data has shown the absence of a daily cycle in cloud cover.

### 5.3.4. Aerosols

Aerosol transport patterns and optical properties over Lampedusa have been extensively studied using ground-based measurements and satellite data (e.g., references [57,61–63]). Measurements of the aerosol optical properties were started at Lampedusa in 1999 using an MFRSR instrument; a CIMEL sunphotometer contributing to AERONET was set up in 2000, although it worked with some discontinuity during the first years of operation. An extended dataset combining these two datasets has been implemented, and a correction scheme has been developed to take into account differences in the field of view of the two instruments [63].

Several studies show that, except for the cases directly influenced by Saharan dust transport events, Lampedusa is characterized by low aerosol optical depth (AOD). When such events are not considered in the statistics the annual mean aerosol optical depth at 870 nm is about 0.09 (as derived from the data by [61]). The distribution of the AOD daily average values at 870 nm for the period 1999–2018 (> 4500 days with measurements) is shown in Figure 12: about 75% of all AOD values at 870 nm are below 0.15, while larger AOD values are measured during sporadic events of Saharan dust transport that have a seasonal cycle and typically last for one or two days [57]. The distribution of Ångström exponent values, which is linked to the particles' dimension, is shown in Figure 12. Cases of pollution transport from the European continent, characterized by small particles, i.e., larger Ångström exponent values [61], are infrequent; values of Ångström exponent below 1 represents 78% of all values.

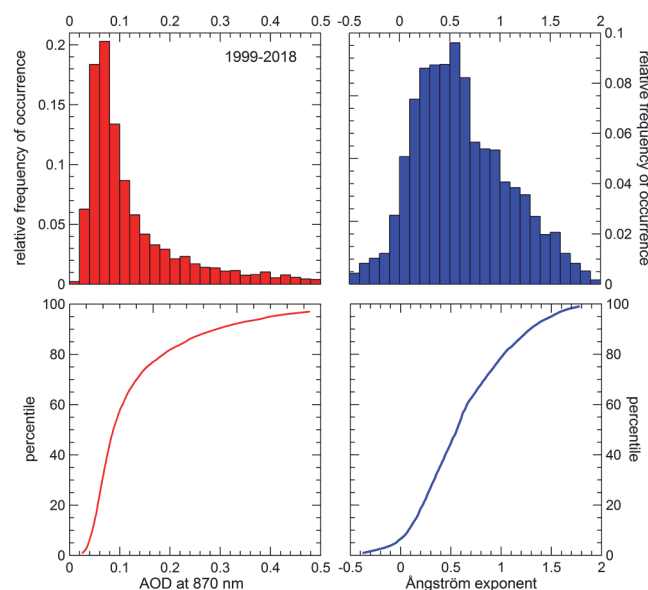


**Figure 12.** Histogram of relative occurrence (**upper**) and cumulative distribution (**lower**) of the values of AOD at 870 nm (**left**) and of the Ångström exponent calculated between 500 nm and 870 nm (**right**). Daily values (> 4500) measured between 1999 and 2018 are used.

Chemical analyses of in-situ aerosol samples [64] show that natural sources (sea salt, mineral dust, and biogenic emissions) give the largest contribution to PM<sub>10</sub> all year round. Sea salt represents the largest absolute and relative contribution in all seasons, with a maximum (54%) in winter and minima (33%) in summer, while desert dust contributes by 17%–37% (largest in autumn).

### 5.3.5. Interfering Gases

Among all the atmospheric gases with absorption in the UV-visible-near infrared spectral intervals, water vapor, ozone, nitrogen dioxide, and sulphur dioxide have the largest absorption.

Total ozone column (TOC) has been measured at Lampedusa since 1998 by means of the Brewer spectrophotometer #123. TOC time series in the period 2000–2016 has a clear annual cycle with

maxima in spring and minima in autumn, which is the result of a balance between transport and photochemical loss, whereby the former is dominant in winter, while photochemical loss dominates in summer, leading to a minimum in autumn. The TOC mean annual cycle at Lampedusa obtained from daily average has an amplitude of about 60 DU. The TOC diurnal variability is mainly caused by photochemical and transport processes occurring in the troposphere. At Lampedusa, diurnal variability is limited, below 2.5% under cloud-free conditions.

The total NO<sub>2</sub> column is not measured at Lampedusa, so data from the Ozone Monitoring Instrument satellite (OMI) onboard Aura satellite have been examined. The temporal evolution of NO<sub>2</sub> column density provided by OMI measurements have been derived in the period 2010–2018 from the NASA Giovanni web site (<https://giovanni.gsfc.nasa.gov/giovanni/>). Maxima are reached in summer and minima in winter, with an amplitude of the annual cycle of about  $2 \times 10^{15}$  cm<sup>-2</sup>. The day-to-day column NO<sub>2</sub> variability is <17%.

Finally, in-situ measurements of O<sub>3</sub> and NO<sub>2</sub> mixing ratio show that their diurnal variability is negligible.

#### 5.4. Adjacency Effect

The contribution of the diffuse radiance reflected by the presence of land to the radiance measured by the satellite for an ocean scene, called the adjacency effect (AE), perturbs the spectral satellite data, thus leading to uncertainties in derived primary products. The AE has to be minimized by considering a minimum distance from the coast (i.e., [12]).

The adjacency radiance contribution depends on the land surface radiative properties (spectral and geometric), on the extension and morphology. The adjacency effect field around Lampedusa island has been studied by [65] simulating OLCI measurements at the central wavelengths of four OLCI channels ( $\lambda = 490$  nm, 555 nm, 670 nm, and 865 nm), accounting for typical surface and atmospheric conditions derived from satellite or remote sensing surface observations.

According to the results of this study, AE is avoided at distances larger than 15 km from the coast of the island.

Since land surface albedo has a key role in the estimation of the AE, spectrally detailed measurements of this quantity should be made at the same time and at the same wavelength as OC measurements [65]. The estimation of the AE will take advantage of surface albedo measurements carried out at the Atmospheric Observatory. While spectral downward irradiance has been measured by spectroradiometers since 2013, measurements of reflected spectral irradiance are about to be started.

Measurements of broadband solar albedo at the Atmospheric Observatory started in 2016. The annual distribution of the surface albedo monthly mean values presents maxima of 0.19–0.21 from July to January, and a decrease to 0.16–0.17 in April and May, when the occurrence of rain favors the growth of vegetation, decreasing the reflecting properties of the surface.

## 6. Uncertainty Budget

### 6.1. Uncertainty of the Radiometric Measurement

The estimated uncertainty budget (EUB) of the infrastructure is firstly assessed for the radiometric measurements. For each radiometric correction, the measurement equation is implemented in the ground segment to provide end-to-end uncertainties of every individual measurement (Figure 13). Uncertainty propagation is then theoretically achievable with this formalism (Type A uncertainty, defined in a statistical sense), using either the Guide to the Expression of Uncertainty in Measurement (GUM) first-order assumption [66] or Monte Carlo simulations [67].

For the quantified EUB of the optical system, we prefer, however, to rely on the actual uncertainties recently assessed by the MOBY team with the MarONet optical system [17,18]. This refers to Type B uncertainties, i.e., uncertainties not derived by a statistical analysis, but field experiences, calibration reports, and background knowledge on the system. It shall be noted that uncertainties of



MarONet are reduced compared to the previous MOBY system [68]. The EUB of the optical system is split into three main parts:

1. Uncertainty of water-leaving radiance ( $L_w(0^+)$ ) covering the optical system (Table 4), deployment structure and ground segment processing (Table 5);
2. Uncertainty of the downwelling irradiance ( $E_d$ ) covering the optical system and environmental effects (Table 6);
3. Uncertainty of the resulting remote-sensing reflectance,  $R_{rs}$  (Table 7).

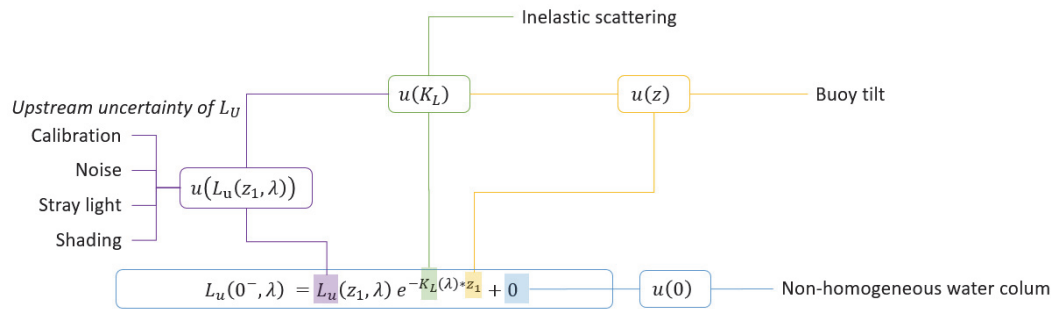


**Figure 13.** Example of measurement equation for uncertainty propagation:  $L_u$  depth propagation.

A basic principle in the uncertainty budget is that corrections are multiplicative. The formalism adopted in the study follows the protocols of the IOCCG report “Protocols for Satellite Ocean Color Data Validation: In-situ Optical Radiometry” [28]. Denoting with the symbol  $\mathfrak{J}(\lambda)$  either  $L(\lambda)$  or  $E(\lambda)$  in physical units ( $W \cdot cm^{-2} \cdot sr^{-1} \cdot nm^{-1}$  and  $W \cdot cm^{-2} \cdot nm^{-1}$ , respectively), the conversion equation for a given correction,  $\mathfrak{N}_i(\lambda)$ , from measurement  $\mathfrak{J}_{i-1}$  to measurement  $\mathfrak{J}_i$ , is

$$\mathfrak{J}_i(\lambda) = \mathfrak{N}_i(\lambda) \cdot \mathfrak{J}_{i-1}(\lambda) \tag{9}$$

The term  $\mathfrak{N}_i(\lambda)$  accounts for the non-ideal instrument response of the instrument and implicitly depends on various input parameters (possibly other wavelengths, like for straylight correction). The final radiometry is thus given by the product of all corrections:

$$\mathfrak{J}(\lambda) = \prod_{i=1}^N \mathfrak{N}_i(\lambda) \cdot \mathfrak{J}_0(\lambda) \tag{10}$$

where  $\mathfrak{J}_0$  represents the net radiometric data obtained by subtracting the dark contribution from signal data after scaling the raw CCD readouts by the measurement integration time and the bin factor. Applications of the GUM gives

$$\frac{u^2(\mathfrak{J}(\lambda))}{\mathfrak{J}(\lambda)^2} = \sum_{i=1}^N \frac{u^2(\mathfrak{N}_i(\lambda))}{\mathfrak{N}_i(\lambda)^2} + \frac{u^2(\mathfrak{J}_0(\lambda))}{\mathfrak{J}_0(\lambda)^2} \tag{11}$$

This justifies why the quadratic uncertainty budget is additive, in relative unit, in the next tables. Furthermore, the tables tentatively distribute the uncertainties sources between their random and systematic parts. This has an important consequence on the SVC gains, further discussed in the next section.

**Table 4.** The estimated uncertainty budget (EUB) of the in-situ optical system (Lu), in %. See text for justification on the numbers.

Requirement from [3]	Uncertainty Source	Uncertainty Type (A/B)	412 nm		443 nm		490 nm		560 nm		674 nm	
			rand.	syst.	rand.	syst.	rand.	syst.	rand.	syst.	rand.	syst.
OC-VCAL-RD-14	Spectral resolution											
OC-VCAL-RD-15	Spectral calibration	B		0.38		0.29		0.22		0.14		0.06
OC-VCAL-RD-16	Stray-light	B		0.18		0.06		0.02		0.06		0.04
OC-VCAL-RD-17	Radiometric calibration	B		0.81		0.72		0.61		0.53		0.46
		B		0.42		0.46		0.51		0.53		0.49
		B	0.20		0.20		0.20		0.20		0.20	
		A	0.51		0.21		0.22		0.12		0.10	
		B		0.20		0.15		0.03		0.03		0.03
OC-VCAL-RD-18	Angular response											
OC-VCAL-RD-19	Immersion factor	B	0.05		0.05		0.05		0.05		0.05	
OC-VCAL-RD-20	Thermal stability	B	0.16		0.16		0.16		0.16		0.16	
OC-VCAL-RD-21	Dark current											
OC-VCAL-RD-22	Polarisation sensitivity	B	0.20		0.20		0.20		0.20		0.20	
OC-VCAL-RD-23	Non-linearity response											
OC-VCAL-RD-24	Noise characterisation	B	0.15		0.15		0.15		0.15		0.15	
		B	1.43		1.12		0.95		0.87		0.74	
OC-VCAL-RD-25	Environ. conditions (like-to-like rule)	B	1.65		1.37		1.69		1.82		1.25	
Total uncertainty on optical system Lu			2.27	1.02	1.82	0.92	1.99	0.82	2.05	0.77	1.50	0.68
<b>Total uncertainty on optical system Lu (rand. + syst.)</b>			<b>2.49</b>		<b>2.04</b>		<b>2.15</b>		<b>2.19</b>		<b>1.65</b>	

**Table 5.** EUB of the deployment structure (Lu in the field) and ground segment up to Lw(0+), in %. See text for justification on the numbers.

Requirement from [3]	Uncertainty Source	Uncertainty Type (A/B)	412 nm		443 nm		490 nm		560 nm		674 nm	
			rand.	syst.	rand.	syst.	rand.	syst.	rand.	syst.	rand.	syst.
<b>Deployment structure (Lu)</b>												
OC-VCAL-RD-26	Shading	A		0.50		0.50		0.60		1.25		4.00
OC-VCAL-RD-27	Tilting & BRDF	A	0.20		0.20		0.20		0.20		0.20	
	Environmental fluctuation	B	0.10		0.10		0.10		0.15		0.20	
OC-VCAL-RD-49	Bio-fouling	A	1.00		1.00		1.00		1.00		1.00	
<b>Ground segment up to in-situ Lw(0+)</b>												
OC-VCAL-RD-28	Depth-extrapolation	A		0.40		0.40		0.40		0.40		0.40
OC-VCAL-RD-29	Surface propagation	A		0.10		0.10		0.10		0.10		0.10
OC-VCAL-RD-30	Data reduction	A	2.00		2.00		2.00		3.00		3.00	
Total uncertainty on in-situ Lw(0+)			3.20	1.21	2.89	1.12	3.00	1.10	3.78	1.52	3.51	4.08
<b>Total uncertainty on in-situ Lw(0+) (rand. + syst.)</b>			<b>3.42</b>		<b>3.10</b>		<b>3.19</b>		<b>4.07</b>		<b>5.38</b>	

**Table 6.** EUB of in-situ Es, in %. See text for justification on the numbers.

Requirement from [3]	Uncertainty Source	Uncertainty Type (A/B)	412 nm		443 nm		490 nm		560 nm		674 nm		
			rand.	syst.	rand.	syst.	rand.	syst.	rand.	syst.	rand.	syst.	
<b>Optical system and ground segment (Es)</b>													
OC-VCAL-RD-33	Spectral calibration	B		0.34		0.25		0.19		0.12		0.06	
	Cosine response	B		0.10		0.10		0.10		0.10		0.20	
	Stray-light	B		1.07		0.35		0.11		0.05		0.27	
	Radiometric calibration	B			0.52		0.46		0.43		0.39		0.34
		B			0.77		0.76		0.69		0.67		0.61
		B			0.49		0.49		0.49		0.49		0.49
		A	0.31		0.14		0.10		0.06		0.06		
	B			0.10		0.10		0.10		0.10		0.10	
	Thermal stability	B		0.16		0.16		0.16		0.16		0.16	
	Noise characterisation	B		0.15		0.15		0.15		0.15		0.15	
		B		1.14		0.92		0.76		0.69		0.53	
Environmental uncertainty	B		2.00		2.00		2.00		2.00		2.00		
Total uncertainty on in-situ Es			2.33	1.54	2.22	1.11	2.15	0.98	2.13	0.93%	2.08	0.92	
<b>Total uncertainty on in-situ Es (rand. + syst.)</b>			<b>2.80</b>		<b>2.48</b>		<b>2.37</b>		<b>2.32</b>		<b>2.27</b>		

**Table 7.** EUB of in-situ remote-sensing reflectance (Rrs), resulting from Tables 5 and 6, in %.

	412 nm		443 nm		490 nm		560 nm		674 nm	
	rand.	syst.	rand.	syst.	rand.	syst.	rand.	syst.	rand.	syst.
<b>Total uncertainty on in-situ Rrs</b>	3.96	1.96	3.64	1.58	3.69	1.47	4.33	1.79	4.08	4.18
<b>Total uncertainty on in-situ Rrs (rand. + syst.)</b>	<b>4.42%</b>		<b>3.97</b>		<b>3.98</b>		<b>4.69</b>		<b>5.84</b>	

Table 4 gives the EUB of the optical system (Lu), and Table 5 gives the EUB of the deployment structure (Lu in the field) and of the depth extrapolation and post-processing up to Lw(0+). Most of the terms are from Voss et al. 2017 and Johnson et al. 2017 [17,18]. Uncertainty due to spectral resolution is covered in the next section. The five sources of uncertainty related to radiometric calibration refer, respectively, to the sphere calibration, sphere drift, non-uniformity, calibration measurement uncertainty and spectral interpolation at the radiometer bands. The effect of angular responses is neglected thanks to very limited FOV (1.73° full angle). The uncertainty of the immersion factor comes from Feinholz et al. 2017 [16]. Thermal stability refers to terms “instantaneous temperature” in Johnson et al. 2017 [18]. Dark current is implicitly taken into account in the temporal averaging and random component of noise calibration below. Uncertainty related to polarization comes from Voss et al. 2017 [17] and is very conservative, considering the use of a depolarizer. Noise characterization covers MOBY integration time and reproducibility of Johnson et al. 2017 [18]. The effect of environmental conditions on Lu is assessed with a very conservative assumption as the sum of uncertainties related to MOBY stability during deployment—system response, in-water internal calibration, and wavelength stability [68].

The quantified uncertainty of the depth propagation at MOBY of 0.4% [17] is kept for EURYBIA. Indeed, with chlorophyll concentration below 0.15 mg/m<sup>3</sup> most of the time relevant for SVC (only up to 0.2 in January), the attenuation coefficient at Lampedusa is below the maximum considered in Voss et al. 2017 [33]; real acquisitions at Lampedusa done with a Satlantic profiler (with OCR507 radiometers) in 2017 confirms values of  $K_L$  below 0.04 m<sup>-1</sup> from 412 nm to 510 nm, of about 0.06 m<sup>-1</sup> at 555 nm and 0.22 m<sup>-1</sup> at 665 nm, fully compatible with the analysis of Voss et al. 2017 [33] at MOBY (see their Figure 6). A conservative uncertainty of 1% is assigned to the biofouling correction [68].

The total uncertainty of Lw(0+) ranges from 3% to 5.5%, with spectral variation essentially due to spectral emission of the calibration lamp and noise level.

EUB of solar irradiance (Es) is given in Table 6. The uncertainty induced by the cosine correction depends on the solar zenith angle and the wavelength. For relevant conditions used in the SVC (most of the time  $\theta_0 < 60^\circ$ ), the uncertainties range from below 0.1% in the blue and green bands to 0.2% in the red. Uncertainty of radiometric calibration accounts for these five sources respectively [18]: FEL lamp calibration, drift, bench effect, calibration measurement uncertainty, and spectral interpolation. The EUB includes also an estimated 2% environmental uncertainty, yielding a total uncertainty between 2% and 3% at all bands.

Table 7 eventually gives the uncertainty of remote-sensing reflectance (Rrs), through simple combination between Lw and Es. We emphasize that the requirement to conduct SVC with Lw rather than  $Rrs = Lw/Es$  is not agreed by all agencies; using Rrs may increase the total EUB and is here considered as a conservative assumption. The total uncertainty remains below 5% from 412 nm to 560 nm and below 6% in the red. These numbers come from various conservative assumptions and provide more an upper threshold than optimal estimates for the EURYBIA concept. Slightly smaller uncertainties can likely be expected during the detailed design of the infrastructure.

## 6.2. Uncertainty of the SVC Gains

The second level of the EUB refers to the SVC process, i.e., uncertainty of the vicarious gains. Although gain computation is not part of the SVC infrastructure, we consider that it is of highest importance to quantify the end-to-end uncertainty of the system. This computation is done for the identified locations around Lampedusa as well as for the MOBY location in Hawaii (MOBY), and using OLCI data and effective criteria defined by EUMETSAT, detailed below. Because both Lampedusa candidate locations yield very similar numbers, in the following we only report the analysis for location LMP1 (East of Lampedusa). The EUB contains two parts, both based on realistic assumption on the number of match-ups and radiometry at the calibration site.

1. Ground segment post-processing for in-situ and satellite data merging in the gain computation, i.e., match-ups, spectral integration (Table 8);



2. Gain computation, up to final mission average gains over a decade (Figure 14).

We cover two years of Sentinel-3 OLCI data (Full Resolution products) from July 2017 to July 2019. We apply the strict criteria used by EUMETSAT for SVC gain generation, assuming that the criteria related to the in-situ measurement should be met with an operational infrastructure:

1.  $5 \times 5$  box centered on single pixels;
2. For each pixel, sensor zenith angle should be below  $56^\circ$  and the sun zenith angle below  $70^\circ$ ;
3. Excluding pixels contaminated by known disturbances, i.e., masked with at least one of the following flags: CLOUD, CLOUD\_AMBIGUOUS, CLOUD\_MARGIN, INVALID, COSMETIC, SATURATED, SUSPECT, HISOLZEN, HIGHGLINT, SNOW\_ICE, WHITECAPS, ANNOT\_ABSO\_D, ANNOT\_MIXR1, ANNOT\_TAU06, RWNEG\_O2, RWNEG\_O3, RWNEG\_O4, RWNEG\_O5, RWNEG\_O6, RWNEG\_O7, RWNEG\_O8;
4. All pixels within the  $5 \times 5$  region of interest (ROI) should be valid;
5. Mean chlorophyll within the ROI should be below  $0.2 \text{ mg/m}^3$ ;
6. Mean aerosol optical depth (AOD) for the channel at 865 nm should be below 0.15;
7. Coefficient of Variation  $CV = \frac{\sigma^*}{\mu^*}$  should be below 0.15 for remote sensing reflectances at bands between 412 and 560 nm, where  $\mu^*$  and  $\sigma^*$  are mean and standard deviation, respectively, computed after the removal of pixel outliers. A pixel is considered as an outlier for variable  $x_i$  if  $|x_i - \mu| < 1.5 \sigma$  where  $\mu$  is the mean and  $\sigma$  is the standard deviation of that variable over the  $5 \times 5$  box.

In two years, the number of valid data is 36 at Lampedusa and 64 at Hawaii (Table 9). The difference is essentially explained by the threshold on AOD, and to a lesser extent on chlorophyll concentration, noticing that the number of match-ups after the flag and geometry screening only is exactly similar (70 match-up in two years for both sites). However, recent analyses suggest that OLCI may overestimate AOD [69], possibly reducing the number of cases for valid matchups at Lampedusa.

In the uncertainty of the ground segment post-processing, our analysis includes the spatial variability of the satellite observation (the first item of Table 8). This uncertainty is quantified for every match-up in each relative unit by the Coefficient of Variation (CV) and strongly grows toward red bands for clear waters. This term appears to be crucial in the EUB; neglecting it would drastically reduce the final uncertainty on the SVC gains in the NIR.

**Table 8.** EUB of the match-up process. See text for justification on the numbers.

Requirement from [3]	Uncertainty Source	Uncertainty Type (A/B)	412 nm		443 nm		490 nm		560 nm		674 nm	
			rand.	syst.	rand.	syst.	rand.	syst.	rand.	syst.	rand.	syst.
OC-VCAL-RD-35-36, 43-44-45	Environmental variability against satellite	A	4.00		3.50		3.60		9.40		56.10	
OC-VCAL-RD-41	Spectral integr. to satellite SRF	A		0.50		0.50		0.50		0.50		0.50
OC-VCAL-RD-42	Normalisation & BRDF corr.	A	1.00	1.00	1.00	1.00	1.00	1.00	1.00	1.00	1.00	1.00
Total uncertainty on targeted Rrs			5.71	2.26	5.15	1.93	5.25	1.85	10.40	2.11	56.26	4.33
<b>Total uncertainty on targeted Rrs (rand. + syst.)</b>			<b>6.14</b>		<b>5.50</b>		<b>5.57</b>		<b>10.61</b>		<b>56.42</b>	

**Table 9.** Number of Ocean and Land Color Instrument (OLCI) match-ups between July 2017 and July 2019 when applying System Vicarious Calibration (SVC) criteria of EUMETSAT.

Criteria	Lampedusa (EURYBIA)	Hawaii (MOBY)
Total number of acquisitions	159	148
100 % valid pixels (flags and geometry)	70 [44%]	71 [48%]
Chl $\leq 0.2$ mg/m <sup>3</sup>	134 [84%]	147 [100%]
AOD(865) $\leq 0.15$	89 [56%]	105 [71%]
CV $< 0.15$ from 412 to 560 nm	95 [60%]	108 [73%]
Combined criteria	36 [23%]	64 [43%]

For a given band  $\lambda$  in the visible part of the solar spectrum, the SVC of OLCI consists first in computing individual gains,  $g(\lambda)$ , for every match-up and pixels [70]:

$$g(\lambda) = \frac{\rho_{path}(\lambda) + t(\lambda) \cdot \rho_w^t(\lambda)}{\rho_{gc}(\lambda)} \quad (12)$$

where  $\rho_w^t(\lambda)$  is the in-situ marine reflectance (de-normalise for BRDF effect, i.e., in the observation and solar geometry of the actual pixel),  $\rho_{path}(\lambda)$  and  $t(\lambda)$  are the atmospheric path reflectance and diffuse total transmittance, respectively, accounting for the Rayleigh and aerosol components reflectance and  $\rho_{gc}(\lambda)$  is the actual TOA reflectance pre-corrected for gaseous absorption and sun glint effect. Note that computation and application of gains directly on the TOA Level-1 radiometry would not change the present analysis. When dealing with standard atmospheric correction [37,71], the aerosol amount and type are identified by the near-infrared (NIR) bands only, assumed to be calibrated beforehand by other means [70]. Application of the GUM first-order assumption [66] gives the uncertainty of individual gain:

$$u(g)^2 = \left(\frac{t\rho_w^t}{\rho_{gc}}\right)^2 \left( \left(\frac{u(\rho_w^t)}{\rho_w^t}\right)^2 + \left(\frac{u(\rho_{path})}{\rho_{path}}\right)^2 \left(\frac{\rho_{path}}{t\rho_w^t}\right)^2 + \left(\frac{u(t)}{t}\right)^2 + \frac{u(\rho_{path}, t)}{t\rho_{path}} \frac{\rho_{path}}{t\rho_w^t} \right) \quad (13)$$

This equation implicitly discards the uncertainty of the satellite radiometry before SVC, i.e.,  $u(\rho_{gc})$ , because it essentially depends on the satellite characteristics (radiometric noise) and not on the OC-SVC infrastructure nor aerosol or marine conditions. In term of covariances, we do not expect either any correlation with  $\rho_{gc}$ , insofar as the standard atmospheric correction does not detect aerosol from the VIS domain:  $r(\rho_{gc}, \rho_{path})=0$  and  $r(\rho_{gc}, t)=0$ . On the contrary, covariance between scattering functions exists and is included through  $u(\rho_{path}, t)$ . The multiplicative factor  $t\rho_w^t/\rho_{gc}$  decreases in absorbing waters and theoretically minimizes the uncertainty of  $g$ . However, complex waters may counterbalance this decrease by an increased uncertainty of the additive components in the square brackets—less reliable in-situ marine reflectance (temporal variability, radiometric measurement) and possibly more complex atmosphere. Also, a lower ratio gives more importance to the atmospheric uncertainty through the factor  $\rho_{path}/t\rho_w^t$ . The balance between all terms is important to get the realistic uncertainty estimate.

Eventually, when the uncertainties of individual gains are computed, the uncertainty on the mission average gains  $\bar{g}$  is simply given by

$$u(\bar{g})^2 = \frac{1}{N^2} \sum_{match-ups} u(g) \quad (14)$$

This formula assumes a simple average of the individual gains. More evolved averaging techniques are also possible, such as the mean of the semi-interquartile range to remove outliers, or a weighted average. In the present context we have no access to the distribution of the gains, only to their

uncertainties, so the arithmetic averaging is kept as a conservative estimate. The value of  $u(\bar{g})$  is affected by the number of years considered in the time-series, here  $Y = 2$ . A more objective metric is the Relative Standard Error of the Mean (RSEM), introduced by Zibordi et al. 2015 [4] to study the stability requirements of SVC gains per decade. With an average SVC gain of the order of unity, RSEM, can be related to our computed  $u(\bar{g})$  by simply scaling the number of match-ups obtained in  $Y$  years to a decade.

$$RSEM = u(\bar{g}) / \sqrt{\frac{10}{Y}} \quad (15)$$

The relative uncertainty of in-situ marine reflectance,  $\frac{u(\rho_w^t)}{\rho_w^t}$ , is assumed to be of 5% at all bands and all calibration sites (Lampedusa, Hawaii). This assumption, previously used in Zibordi et al. 2015 [4], is consistent with the overall quantification detailed in the previous sections. It has obviously a direct impact on the final uncertainties and could be refined in a later stage. The purpose of the present analysis is to simulate the gain uncertainties that would be achieved with OLCI over these locations assuming high-quality and daily radiometric measurements. All other terms involved in the computation of  $u(g)$  are assessed by satellite data, notably the uncertainties of the atmospheric scattering functions,  $u(\rho_{path})$  and  $u(t)$ . This allows conducting a harmonized uncertainty budget for all sites under consideration, while only Lampedusa is fully characterized by long-term AERONET measurements. The choice is made here to fully rely on OLCI aerosol products, as it would be done in real SVC operation. The actual uncertainties  $u(\rho_{path})$  and  $u(t)$  for a given match-up used in the SVC process may be due to many sources, such as the aerosol modelling in the atmospheric correction, the aerosol identification in the NIR, the propagation in the visible, and include both systematic and random components. Because the purpose of SVC is to remove the systematic effects, the present analysis determines  $u(\rho_{path})$  and  $u(t)$  by the local variation of  $\rho_{path}$  and  $t$  around the calibration site. This approach considers that heterogeneity in the atmospheric functions degrades the confidence in the gains. The method is implemented as follows:

1. Consider, for each potential match-up, a ROI of  $5 \times 5$  OLCI pixels (full resolution), consistent with EUMETSAT protocols for SVC as defined previously;
2. Consider all OLCI metadata and ancillary data at pixel level (wind speed, pressure, geometry);
3. Consider OLCI aerosol optical thickness and Angstrom coefficient;
4. Identify, for each pixel, the best matching aerosol model in the OLCI LUTs;
5. Given geometry and ancillary data, compute  $\rho_{path}$  and  $t$  by the OLCI LUTs (Rayleigh + aerosol), as done in OLCI atmospheric correction;
6. Compute  $u(\rho_{path})$  and  $u(t)$  by their local standard-deviation over the ROI.

Final values of RSEM are given in Figure 14—the top-left for Lampedusa (LMP1 location) and the top-right for the Hawaii location. RSEM is of about 0.05% at all bands and both sites, with a peak closer to 0.08% in the Mediterranean at 490 nm. These numbers are consistent with the stability requirement over a decade in the blue-green bands but do not reach the requirement of 0.005% in the red. It is worth noting that this target is hardly reached by any existing SVC infrastructure. Indeed, the RSEM values computed by Zibordi et al. 2015 [4] based on real SVC gains with real in-situ measurements shows that only MOBY gains reach the required RSEM of 0.05% in the blue bands, and not in the red (their Figure 4, reprinted here in Figure 14, bottom-right). Despite the consideration of spatial variability in our uncertainty estimate (more than 50% at 674 nm, Table 8), this strongly suggests that the actual uncertainties of marine reflectance are, for many infrastructures, largely above 5%, especially in the red bands for clear waters.

Another analysis has been conducted in parallel following [4], by simplifying the uncertainty computation of individual gain by  $u(g) = \left( \overline{t\rho_w^t / \rho_{gc}} \right) * u(\rho_w^t) / \rho_w^t$ , where the overline stands for a temporal average. At Lampedusa, this average factor is of 8.4% at 412 nm, 10.7% at 443 nm, 12.4% at 490 nm, 5.6% at 560 nm, and 1.2% at 674 nm. While neglecting the atmospheric uncertainties, this

formulation allows easy computation of the uncertainty of gains, hence of RSEM, for testing various distributions of in-situ uncertainty sources between their random and systematic parts. Here two cases have been investigated:

1. A purely random case: the uncertainty sources are all assigned to the random component.
2. A mix between random and systematic sources (Figure 14, bottom-left, triangles): in Tables 4–8, an attempt is made to assign the uncertainty of various sources to the systematic component, only (i.e., without any random counterpart). Note that the global uncertainty of a given source is identical to the previous case (i.e., the quadratic sum of the random and systematic components equals the square random component of the previous case).

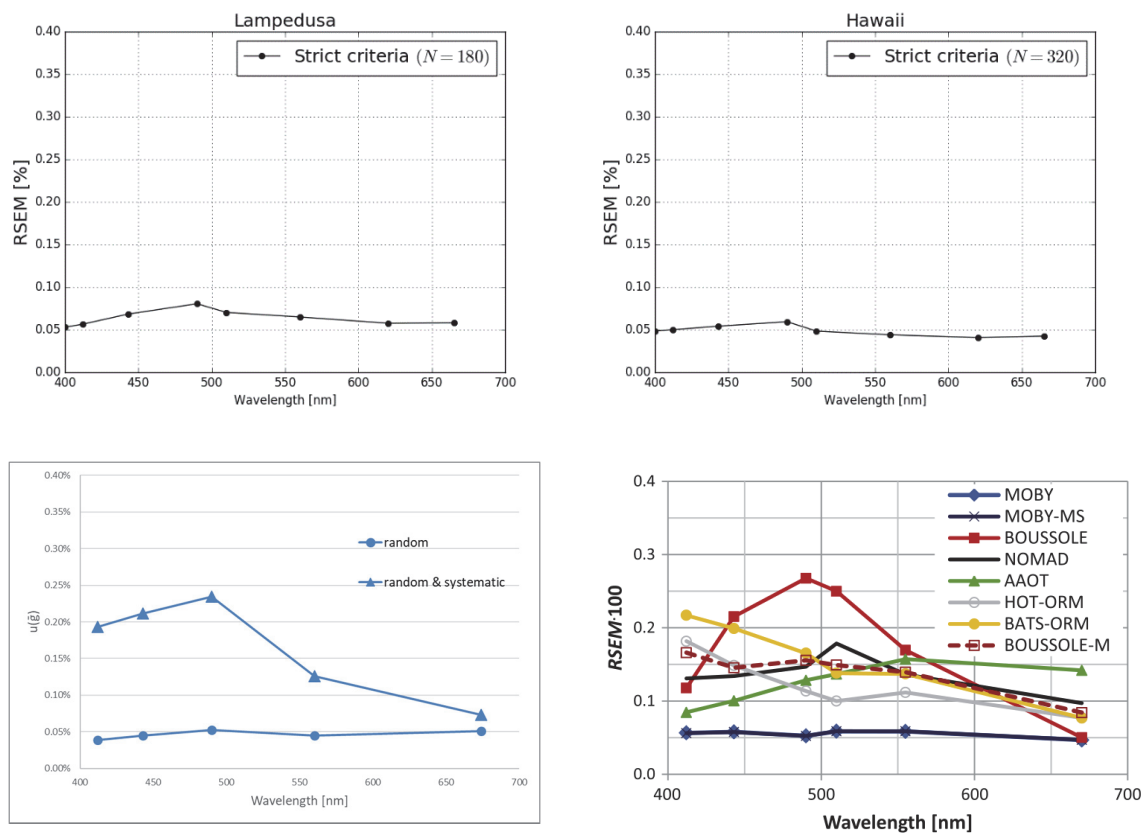


**Figure 14.** Relative Standard Error of the Mean (RSEM) of vicarious gains over a decade as a function of wavelength from various methods. Top: computation from GUM uncertainty propagation and OLCI data at Lampedusa (**left**) and Hawaii (**right**) assuming 5% uncertainty on in-situ Rrs with random source. Bottom left: simplified uncertainty of SVC gains from detailed EUB at Lampedusa (Tables 4–6) accounting for either purely random effects (circles) or both random and systematic effects (triangles; see previous tables for distribution). Bottom right: RSEM measured on real SVC gains computed at various site (MOBY in dark blue) for the SeaWiFS sensor (except BOUSSOLE-M: for MERIS) under a purely random assumption; reprinted from Zibordi et al. 2015 [4].

The first case is an ideal condition, that reduces the uncertainty of mission-average gains as a function of the square root of the number of match-ups. Such an assumption is generally retained in the SVC literature: Antoine et al 1999 [70] and Zibordi et al. 2015 [4] have estimated the final SVC uncertainty through the standard-error of the mean or the relative standard error of the mean of SVC gains, what amounts to dividing the standard-deviation of individual gains by the square root of number of match-ups. Under this purely random assumption, the EURYBIA assessment retrieves an uncertainty of about 0.05% over the full spectral range (Figure 14, bottom-left with circles) which is extremely similar to the assessment of Zibordi et al. 2015 [4] for MOBY (reprint in

Figure 14, bottom-right, blue curve for MOBY). The perfect consistency between these two assessments, made under completely different datasets and methods, is noteworthy—the EURYBIA computation relies on the uncertainty budget of the optical system (MarONet quantification) over Lampedusa conditions observed by OLCI, while the Zibordi et al. 2015 [4] estimate relies on the statistical analysis of real SVC gains computed at MOBY for the SeaWiFS sensor. These results demonstrate the relevance of EURYBIA, based on both the state-of-the-art optical system and favorable conditions, while other systems cannot meet such performance (Figure 14, bottom-right, other systems than MOBY).

This purely random assumption may, however, not be strictly true for various sources of uncertainty. For instance, it is likely that the radiometric calibration, stray light correction, depth extrapolation, have systematic uncertainties. The resulting uncertainty of average gains is then not driven by the number of match-ups, but by these systematic contributions which do not cancel out in the averaging process. Uncertainties can now reach nearly 0.25% in the blue and 0.1% in the red (Figure 14, bottom-left with triangles). Importantly, although these numbers show some similarity with the curves of Zibordi et al. 2015 [4] for non-MOBY systems, they are not comparable in the sense that the relatively poor performance of these latter systems still benefits from the ideal random assumption. We also emphasize that the “rand.+syst.” case refers to the worst case scenario, since all sources should in reality have a random part. The distinction between both components is currently not addressed [18,33] and should be investigated in the next phase. The reality probably lies between the ideal random assumption and the worst-case scenario. Quantifying the detailed structure of the uncertainties is a key scientific challenge that should be addressed by coordinated effort among SVC teams and metrology institutes part of the future OC-SVC network.

In summary, the present analysis based on two years of OLCI data demonstrates that the Lampedusa location (either east or north-west, the latter not shown here) is theoretically suitable for an SVC site, in comparison with the existing site in Hawaii. Clearly, the screening criteria currently defined for an ideal location such as Hawaii removes a lot of data in the Mediterranean Sea (about 48% removal at Lampedusa versus less than 9% at Hawaii, starting from the number of valid data after flag and geometrical screening). However, the amplitude of the marine signal at Lampedusa is below that of the oligotrophic waters of Hawaii (while not being as low as for mesotrophic waters), what advantageously drives the uncertainty propagation from sea level to the SVC gains (term  $t\rho_w^t/\rho_{gc}$ ).

## 7. Discussion and Conclusions

In this paper, we presented the overall design of the EURYBIA OC-SVC infrastructure, taking into account the Copernicus long-term and multi-mission perspective to deliver OC products and services.

Our strategy, to reach the goal to deliver state-of-the-art Fiducial Reference Measurements (FRM) in a very tight development schedule (expected operational target after 36 months from the beginning of the development), is to operate independently but in compliance with MarONet specification [72]. This solution brings to a network concept (e.g., AERONET-OC, [73]) and takes full advantage of more than 30 years of MOBY experience in operation and technological developments. EURYBIA will be compatible with the MarONet network in terms of radiometric data collection, traceability, and protocols, but autonomous regarding detailed architecture, development, funding, and operations.

Our proposed solution for the European OC-SVC Infrastructure (Figure 1) offers the possibility to develop and deploy a technologically proven system within a realistic timeframe for the Copernicus needs. Moreover, it allows to avoid the compatibility issues experienced in the past two decades due to the adoption of different instrumentation and processing approaches.

The MarONet optical system, constituting the core instrumentation of the infrastructure, has been verified to be fully compliant with the radiometric and spectral requirements ([3], see Table 1). The EURYBIA Field Segment accounts for the instrumentation, infrastructure and operations required to acquire radiometric FRM in the field. The field segment includes also an on-shore laboratory for pre- and post-deployment instrument calibration, characterization, and verification of the calibration sources'



stability. Complete SI traceability will be insured by a Metrology Institute. The EURYBIA Ground Segment communicates with the buoys to transmit/receive data and to monitor the infrastructure status ensuring operations on 24/7/365. The processing unit computes data products with their associated uncertainties and performs the quality assurance of results. Data products are distributed within the official Copernicus mechanism through the dissemination unit, which also gives access to the open-source processing code and documentation.

The EURYBIA infrastructure is proposed to be settled in the Strait of Sicily offshore of Lampedusa Island, one of the potential European OC-SVC sites [11–13]. Lampedusa is a small flat island in the central Mediterranean Sea far away from the mainland and main traffic routes, but very well connected to Europe. The island is surrounded by oligotrophic waters and hosts a Marine Protected Area.

Our analysis, based on satellite and in-situ observations, revealed the occurrence of consistent and homogeneous cloud free conditions (> 60% during summer). The median value of the AOD at 870 nm is <0.1, hence below the currently adopted threshold value (0.15) for acceptance of measurements for vicarious calibration. Sporadic larger values of AOT are observed only during desert dust transport events characterized by relatively short time duration (1–2 days) over the whole Mediterranean region [74].

Being Lampedusa a very small island characterized by low and smooth topography, its meteorological conditions are dominated by synoptic scale phenomena, and local effects are negligible, as demonstrated by the absence of a diurnal cycle in cloudiness and aerosol load. Wind patterns are driven by the main synoptic structures, showing prevailing directions from NW, with a limited interannual variability and most frequent wind speed between 4 m/s and 8 m/s. Wave and current conditions are suitable to ensure the required stability of the optical buoy.

The analysis of the optical characteristics of the waters surrounding the Island were compared with those observed at the MOBY site. This reveals that in Lampedusa the annual average chlorophyll is <0.08 mg m<sup>-3</sup>, with a day-to-day and local spatial variability below 10%. An end-to-end uncertainty budget based on OLCI data adopting EUMETSAT screening protocols for SVC and site characterization demonstrates the relevance of this site. The overall uncertainty of EURYBIA SVC gains is estimated to be about 0.05% per decade in the blue-green wavelengths. This value is comparable with those estimated for the reference site in Hawaii and in compliance with stability requirements for climate studies in this spectral domain.

We propose to settle the location site at more than 15 km off the island of Lampedusa at suitable sea depth conditions (> 300m) to avoid adjacency and bathymetry effects. Two candidate locations (Figure 5), satisfying these geophysical criteria and relatively distant from the main marine traffic routes, have been identified—LMP1 (35.5248°N–12.7667°E) and LMP2 (35.7430°N–12.3579°E). Both candidate sites have been evaluated to be fully compliant with the environmental (e.g., cloudiness, aerosols, surface wind, currents, and waves) and logistical requirements for vicarious calibration identified by Mazeran et al. [3]. Recently, Bulgarelli and Zibordi [13] carried out a complete study on the adjacency effect of the Lampedusa Island to address implications on a hypothetical nearby system vicarious calibration infrastructure for satellite ocean color sensors. Their results, as expected, confirmed that the site should be located at distances larger than approximately 14 km from the coast (requirement satisfied by both LMP1 and LMP2). They also suggested that the region in the direction of the reflected sunbeam should be avoided. Based on this latter recommendation LMP1 location should be preferred. The final selection of the exact location where to deploy the optical buoy will require further studies on logistics and environmental characterization, including analyses of ad-hoc in-situ observation to be carried out around the Island. This will be part of future studies to be carried out in phase 3 of the EUMETSAT Programme.

It is important to underline that the EURYBIA design is modular—any update of individual subsystems will be possible without the need to reconsider the whole system architecture. The proposed infrastructure will be able to host, on the moored buoy, additional instrumentation that can be used also for CAL/VAL of other satellite missions. The scheduled cruises for infrastructure maintenance

will give an additional opportunity to collect in-situ measurements needed to improve the current OC product algorithms as well as to develop new ones.

Our EURYBIA design is independent from the proposed installation site, so other potential locations for its deployment could be considered. A preliminary analysis of other potential sites was carried out during the EUMETSAT project (not shown) revealing that Lampedusa is a very good candidate for the installation of the European OC-SVC Infrastructure, also in comparison to other locations. A detailed evaluation of other potential European sites will require a deep inter-comparison of environmental characteristics, including a complete evaluation of end-to-end uncertainty budget as we carried out for Lampedusa and MOBY. This will be part of our future studies.

In conclusion, the logistics, the capability and required expertise to operate the infrastructure will be ensured by the fact that Lampedusa has been hosting a long-term well-established Climate Observatory for more than twenty years. In addition, the presence of the Climate Observatory has the advantage to make available relevant observations on atmospheric variables, including aerosols profiles that could be used to improve the accuracy of system vicarious calibration. Lampedusa, as proposed site, represents a trade-off between ideal conditions reached in Hawaii, for the reference MOBY infrastructure, and the priority to host the EURYBIA system in European waters.

**Author Contributions:** Conceptualization, R.S., G.L.L., D.D., C.M., and A.d.S.; formal analysis, S.C., C.Y., A.P., C.M., G.V., L.C., D.D., A.d.S., and D.M.; data curation, S.C., G.V., T.K., and F.Z.; writing—original draft preparation, G.L.L., M.Y., K.V., R.B., D.M., D.D., A.d.S. and C.M.; writing—review and editing, G.L.L., C.C., D.D., C.M., K.V., and R.S.; supervision, R.S.; project administration, C.C.; funding acquisition, R.S. All authors have read and agreed to the published version of the manuscript.

**Funding:** The development of the EURYBIA concept and its preliminary design have been supported by EUMETSAT and the European Union through project Preliminary Design of the Copernicus Ocean Colour Vicarious Calibration under contract EUM/CO/18/4600002161/EJK. MarONet will be supported by NASA, while MOBY-Refresh, on which the optical system is based, is supported by NOAA.

**Acknowledgments:** The SVC design greatly benefited from comments of the review panel composed by M. Wang, B. C. Johnson, A. Reppucci, G. Zibordi, R. Gilmore, K. N. Babu, and EUMETSAT Team Members composed by E. Kwiatkowska, F. Montagner, I. Cazzaniga, E. Obligis, J. Chimot, and D. Dessailly. The MOBY team (B. C. Johnson, M. Feinholtz, A. Gleason, S. Flora, T. Houlihan, M. Yarbrough, and K. Voss) contributed to the design and construction of MOBY-Refresh. Contributions by C. Bommarito and D. Sferlazzo are gratefully acknowledged. V. Artale and S. Marullo are thanked for making available temperature and salinity data from the Lampedusa Oceanographic Observatory. Analyses of OMI NO<sub>2</sub> data used in this paper were produced with the Giovanni online data system (<https://giovanni.gsfc.nasa.gov/giovanni/>). developed and maintained by the NASA GES DISC. This study has been conducted using EU Copernicus Marine Service Information.

**Conflicts of Interest:** The authors declare no conflict of interest.

## Abbreviations

ACTRIS	Aerosol, Clouds and Trace Gases
ADCP	Acoustic Current Doppler profiler
ADU	Analog Digital Counts
AE	Adjacency Effect
AERONET	Aerosol Robotic Network
AOD	Aerosol Optical Depth
AOT	Aerosol Optical Thickness
BOUSSOLE	BOUée pour l’acquiSition d’une Série Optique à Long termeE
BRDF	Bidirectional Reflectance Distribution Function
BSG	Blue Spectro Graph
C3S	Copernicus Climate Change Service
CCD	Charged Coupled Device
CDOM	Coloured Dissolved Organic Matter
CF	Cloud Fraction
CMEMS	Copernicus Marine Environment Monitoring Service
CTD	Conductivity Temperature Depth
CTP	Cloud Top Pressure

CV	Coefficient of Variation
ESA	European Space Agency
EUB	Estimated Uncertainty Budget
EUMETSAT	European Organisation for the Exploitation of Meteorological Satellites
EURYBIA	EUropean RadiometrY Buoy and InfrAstructure
FOV	Field of View
FRM	Fiducial Reference Measurements
FWHM	Full Width at Half Maximum
GS	Ground Segment
GUM	Guide to the expression of Uncertainty in Measurement
ICOS	Integrated Carbon Observation System
IOCCG	International Ocean Colour Coordinating Group
IOPs	Inherent Optical Properties
LUT	Look-up Tables
MarONet	Marine Optical Network
MC	Monte Carlo
MFRSR	Multi Filter Rotating Shadowband Radiometer
MOBY	Marine Optical BuoY
MODIS	Moderate Resolution Imaging Spectroradiometer
NASA	National Aeronautics and Space Administration
NIR	Near-Infrared
NMI	National Metrology Institute
NOAA	National Oceanic and Atmospheric Administration
NRT	Near Real-Time
OC-SVC	Ocean Colour System Vicarious Calibration
OLCI	Ocean and Land Colour Instrument
OMI	Ozone Monitoring Instrument
PACE	Plankton, Aerosol, Cloud, ocean Ecosystem
PDC	Post-Deployment Calibration
PM10	Particulate Matter smaller than 10µm
QC/QA	Quality Control / Quality Assurance
ROI	Region of Interest
RSEM	Relative Standard Error of the Mean
RSG	Red Spectro Graph
S3	Sentinel-3
SDY	Sequential Day of the Year
SI	International System of Units
SeaWiFS	Sea-viewing Wide Field-of-view Sensor
SRF	Spectral Response Function
SST	Sea Surface Temperature
TCS	Traceable to Calibration Standards
TOA	Top Of Atmosphere
TOC	Total Ozone Column
UTC	Coordinated Universal Time
VIIRS	Visible Infrared Imaging Radiometer Suite
VPH	Volume Phase Holographic

## References

1. Ansper, A.; Alikas, K. Retrieval of Chlorophyll a from Sentinel-2 MSI data for the European Union water framework directive reporting purposes. *Remote Sens.* **2018**, *11*, 64. [[CrossRef](#)]
2. Groom, S.; Sathyendranath, S.; Ban, Y.; Bernard, S.; Brewin, R.; Brotas, V.; Brockmann, C.; Chauhan, P.; Choi, J.; Chuprin, A.; et al. Satellite ocean colour: Current status and future perspective. *Front. Mar. Sci.* **2019**, *6*, 485. [[CrossRef](#)]

3. Mazeran, C.; Brockmann, C.; Ruddick, K.; Voss, K.J.; Zagolsky, F.; Antoine, D.; Bialek, A.; Brando, V.; Donlon, C.; Franz, B.A.; et al. Requirements for Copernicus Ocean Colour Vicarious Calibration Infrastructure; EUMETSAT Study. 2017. Available online: [https://www.eumetsat.int/website/wcm/idc/idcplg?IdcService=GET\\_FILE&dDocName=PDF\\_COP\\_OCEAN\\_COL\\_CAL&RevisionSelectionMethod=LatestReleased&Rendition=Web](https://www.eumetsat.int/website/wcm/idc/idcplg?IdcService=GET_FILE&dDocName=PDF_COP_OCEAN_COL_CAL&RevisionSelectionMethod=LatestReleased&Rendition=Web) (accessed on 28 February 2020).
4. Zibordi, G.; Mélin, F.; Voss, K.J.; Johnson, B.C.; Franz, B.A.; Kwiatkowska, E.; Huot, J.-P.; Wang, M.; Antoine, D. System vicarious calibration for ocean color climate change applications: Requirements for in-situ data. *Remote Sens. Environ.* **2015**, *161*, 361–369. [[CrossRef](#)]
5. Lerebourg, C.; Vendt, R.; Donlon, C. Fiducial reference measurements for satellite ocean colour (FRM4SOC). In *Proceedings of the D-240 Proceedings of WKP-1 (PROC-1) Report of the International Workshop*; European Space Agency: ESRIN: Frascati, Italy, 2016.
6. Gordon, H.R. In-orbit calibration strategy for ocean color sensors. *Remote Sens. Environ.* **1998**, *63*, 265–278. [[CrossRef](#)]
7. IOCCG. *International Network for Sensor Inter-Comparison and Uncertainty Assessment for Ocean Color Radiometry (IN-SITU-OCR)*; International Ocean Color Coordinating Group: Dartmouth, NS, Canada, 2012.
8. Donlon, C. *Sentinel-3 Mission Requirements Traceability Document (MRTD)*; European Space Agency: Noordwijk, The Netherlands, 2011.
9. Clark, D.K.; Yarbrough, M.; Feinholz, M.; Flora, S.; Broenkow, W.; Johnson, C.B.; Brown, S.W.; Yuen, M.; Mueller, J. MOBY, a radiometric buoy for performance monitoring and vicarious calibration of satellite ocean color sensors: Measurement and data analysis protocols. In *Ocean Optics Protocols for Satellite Ocean Color Sensor Validation, Revision 3, Volume 2*; Mueller, J.L., Fargion, G.S., Eds.; NASA Goddard Space Flight Center: Greenbelt, MD, USA, 2002; Volume NASA/TM-2002-21004, pp. 138–170.
10. Antoine, D.; Guevel, P.; Desté, J.-F.; Bécu, G.; Louis, F.; Scott, A.J.; Bardey, P. The “boussole” buoy—A new transparent-to-swell taut mooring dedicated to marine optics: Design, tests, and performance at sea. *J. Atmos. Ocean. Technol.* **2008**, *25*, 968–989. [[CrossRef](#)]
11. Zibordi, G.; Mélin, F. An evaluation of marine regions relevant for ocean color system vicarious calibration. *Remote Sens. Environ.* **2017**, *190*, 122–136. [[CrossRef](#)]
12. Zibordi, G.; Mélin, F.; Talone, M.; European Commission; Joint Research Centre. *System Vicarious Calibration for Copernicus Ocean Colour Missions: Updated Requirements and Recommendations for a European Site*; Publications Office of the European Union: Brussels, Belgium, 2017; ISBN 978-92-79-75340-4.
13. Bulgarelli, B.; Zibordi, G. Adjacency radiance around a small island: Implications for system vicarious calibrations. *Appl. Opt.* **2020**, *59*, C63–C69. [[CrossRef](#)]
14. EUMETSAT. *Sentinel-3 OLCI Marine User Handbook, Version 1H, Ref. EUM/OPS-SEN3/MAN/17/907205*; Technical Report; EUMETSAT: Darmstadt, Germany, 2018.
15. Voss, K.J.; Yarbrough, M.A.; Johnson, B.C.; Feinholz, M.E.; Gleason, A.; Flora, S.J. *Present Status of the Marine Optical Buoy (MOBY) Refresh and MOBY-Net*; MOBY: Dubrovnik, Croatia, 2018.
16. Feinholz, M.; Johnson, C.B.; Voss, K.; Yarbrough, M.; Flora, S. Immersion coefficient for the Marine Optical Buoy (MOBY) radiance collectors. *J. Res. Natl. Inst. Stand. Technol.* **2017**, *122*, 1–9. [[CrossRef](#)]
17. Voss, K.J.; Johnson, C.B.; Yarbrough, M.A.; Gleason, A.; Flora, S.J.; Feinholz, M.E.; Peters, D.; Houlihan, T.; Mundell, S.; Yarbrough, S. An overview of the Marine Optical Buoy (MOBY): Past, present and future. In *Proceedings of the D-240 FRM4SOC-PROC1 Proceedings of WKP-1 (PROC-1) Fiducial Reference Measurements for Satellite Ocean Colour (FRM4SOC)*, Tartu, Estonia, 8–13 May 2017.
18. Johnson, B.C.; Voss, K.J.; Yarbrough, M.A.; Flora, S.J.; Feinholz, M.E.; Peters, D.; Houlihan, T.; Mundell, S. MOBY radiometric calibration and associated uncertainties. In *Proceedings of the D-240 FRM4SOC-PROC1 Proceedings of WKP-1 (PROC-1) Fiducial Reference Measurements for Satellite Ocean Colour (FRM4SOC)*, Tartu, Estonia, 8–13 May 2017.
19. Barden, S.C.; Arns, J.A.; Colburn, W.S. *Volume-Phase Holographic Gratings and Their Potential for Astronomical Applications*; D’Odorico, S., Ed.; SPIE: Kona, HI, USA, 1998; pp. 866–876. [[CrossRef](#)]
20. Flora, S.J.; Broenkow, W.W. Data Reduction Algorithms for the Marine Optical Buoy and Marine Optical System; Moss Landing Marine Laboratories Technical Publication 08-X Moss Landing, CA 95039. 2008, p. 16. Available online: [http://data.moby.mlml.calstate.edu/timeseries/other\\_reports/data%20reduction%20algorithms%20for%20the%20marine%20optical%20buoy.pdf](http://data.moby.mlml.calstate.edu/timeseries/other_reports/data%20reduction%20algorithms%20for%20the%20marine%20optical%20buoy.pdf) (accessed on 28 February 2020).

21. Vabson, V.; Kuusk, J.; Ansko, I.; Vendt, R.; Alikas, K.; Ruddick, K.; Ansper, A.; Bresciani, M.; Burmester, H.; Costa, M.; et al. Laboratory intercomparison of radiometers used for satellite validation in the 400–900 nm range. *Remote Sens.* **2019**, *11*, 1101. [[CrossRef](#)]
22. Zibordi, G.; Talone, M.; Jankowski, L. Response to temperature of a class of in-situ hyperspectral radiometers. *J. Atmos. Ocean. Technol.* **2017**, *34*, 1795–1805. [[CrossRef](#)]
23. Torrecilla, E.; Pons, S.; Vilaseca, M.; Piera, J.; Pujol, J. Stray-light correction of in-water array spectroradiometers. Effects on underwater optical measurements. In Proceedings of the OCEANS 2008, Quebec City, QC, Canada, 15–18 September 2008; pp. 1–5. [[CrossRef](#)]
24. Feinholz, M.E.; Flora, S.J.; Yarbrough, M.A.; Lykke, K.R.; Brown, S.W.; Johnson, B.C.; Clark, D.K. Stray light correction of the marine optical system. *J. Atmos. Ocean. Technol.* **2009**, *26*, 57–73. [[CrossRef](#)]
25. Talone, M.; Zibordi, G.; Ansko, I.; Banks, A.C.; Kuusk, J. Stray light effects in above-water remote-sensing reflectance from hyperspectral radiometers. *Appl. Opt.* **2016**, *55*, 3966. [[CrossRef](#)] [[PubMed](#)]
26. Seckmeyer, G.; Bernhard, G. *Cosine Error Correction of Spectral UV-Irradiances*; Stamnes, K.H., Ed.; SPIE: Tromsø, Norway, 1993; pp. 140–151. [[CrossRef](#)]
27. Zibordi, G.; Bulgarelli, B. Effects of cosine error in irradiance measurements from field ocean color radiometers. *Appl. Opt.* **2007**, *46*, 5529–5538. [[CrossRef](#)] [[PubMed](#)]
28. Zibordi, G.; Voss, K.J.; Johnson, C.B.; Mueller, J.L. Protocols for satellite ocean colour data validation. *In-Situ Opt. Radiom.* **2019**, *3*. [[CrossRef](#)]
29. D’Alimonte, D.; Zibordi, G.; Kajiyama, T. Effects of integration time on in-water radiometric profiles. *Opt. Express* **2018**, *26*, 5908. [[CrossRef](#)] [[PubMed](#)]
30. Kajiyama, T.; D’Alimonte, D.; Cunha, J.C. A high-performance computing framework for Monte Carlo ocean color simulations. *Concurr. Comput. Pract. Exp.* **2017**, *29*, e3860. [[CrossRef](#)]
31. D’Alimonte, D.; Kajiyama, T. Effects of light polarization and waves slope statistics on the reflectance factor of the sea surface. *Opt. Express* **2016**, *24*, 7922. [[CrossRef](#)]
32. Mueller, J.L. *Reduced Uncertainties in Measurements of Water-Leaving Radiance, and Other Optical Properties, Using Radiative Transfer Models and Empirical Data Analysis*; CHORS, San Diego State University Research Foundation: San Diego, CA, USA, 2007.
33. Voss, K.J.; Gordon, H.R.; Flora, S.; Johnson, B.C.; Yarbrough, M.; Feinholz, M.; Houlihan, T. A method to extrapolate the diffuse upwelling radiance attenuation coefficient to the surface as applied to the Marine Optical Buoy (MOBY). *J. Atmos. Ocean. Technol.* **2017**, *34*, 1423–1432. [[CrossRef](#)]
34. Austin, R.W. The remote sensing of spectral radiance from below the ocean surface. In *Optical Aspects of Oceanography*; Jerlov, N.G., Steemann-Nielsen, E., Eds.; Academic Press Inc.: London, UK, 1974; pp. 317–344.
35. Gordon, H.R.; Morel, A.Y. *Remote Assessment of Ocean Color for Interpretation of Satellite Visible Imagery: A Review*; Springer: New York, NY, USA, 2010; ISBN 978-1-118-66370-7.
36. Voss, K.J.; Flora, S. Spectral dependence of the seawater–air radiance transmission coefficient. *J. Atmos. Ocean. Technol.* **2017**. [[CrossRef](#)]
37. Gordon, H.R.; Wang, M. Influence of oceanic whitecaps on atmospheric correction of ocean-color sensors. *Appl. Opt.* **1994**, *33*, 7754. [[CrossRef](#)]
38. Morel, A.; Antoine, D.; Gentili, B. Bidirectional reflectance of oceanic waters: Accounting for raman emission and varying particle scattering phase function. *Appl. Opt.* **2002**, *41*, 6289. [[CrossRef](#)] [[PubMed](#)]
39. Werdell, P.J.; Behrenfeld, M.J.; Bontempi, P.S.; Boss, E.; Cairns, B.; Davis, G.T.; Franz, B.A.; Gliese, U.B.; Gorman, E.T.; Hasekamp, O.; et al. The plankton, aerosol, cloud, ocean ecosystem mission: Status, science, advances. *Bull. Am. Meteorol. Soc.* **2019**, *100*, 1775–1794. [[CrossRef](#)]
40. Grasso, M.; Pedley, H.M. The pelagian islands: A new geological interpretation from sedimentological and tectonic studies and its bearing on the evolution of the central Mediterranean Sea (Pelagian Block). *Geol. Romana* **1985**, *24*, 13–34.
41. Ciardini, V.; Contessa, G.M.; Falsaperla, R.; Gómez-Amo, J.L.; Meloni, D.; Monteleone, F.; Pace, G.; Piacentino, S.; Sferlazzo, D.; Sarra, A. di Global and Mediterranean climate change: A short summary. *Annali Dell’Istituto Superiore Di Sanità* **2016**. [[CrossRef](#)]
42. di Sarra, A.; Bommarito, C.; Anello, F.; Di Iorio, T.; Meloni, D.; Monteleone, F.; Pace, G.; Piacentino, S.; Sferlazzo, D. Assessing the quality of shortwave and longwave irradiance observations over the ocean: One year of high-time-resolution measurements at the Lampedusa oceanographic observatory. *J. Atmos. Ocean. Technol.* **2019**, *36*, 2383–2400. [[CrossRef](#)]



43. Casasanta, G.; di Sarra, A.; Meloni, D.; Monteleone, F.; Pace, G.; Piacentino, S.; Sferlazzo, D. Large aerosol effects on ozone photolysis in the Mediterranean. *Atmos. Environ.* **2011**, *45*, 3937–3943. [[CrossRef](#)]
44. di Sarra, A.; Fua, D.; Cacciani, M.; Di Iorio, T.; Disterhoft, P.; Meloni, D.; Monteleone, F.; Piacentino, S.; Sferlazzo, D. Determination of ultraviolet cosine-corrected irradiances and aerosol optical thickness by combined measurements with a Brewer spectrophotometer and a multifilter rotating shadowband radiometer. *Appl. Opt.* **2008**, *47*, 6142. [[CrossRef](#)]
45. Meloni, D.; Di Biagio, C.; di Sarra, A.; Monteleone, F.; Pace, G.; Sferlazzo, D.M. Accounting for the solar radiation influence on downward longwave irradiance measurements by pyrgeometers. *J. Atmos. Ocean. Technol.* **2012**, *29*, 1629–1643. [[CrossRef](#)]
46. Harrison, A.W.; Coombes, C.A. Performance validation of the Gueymard sky radiance model. *Atmos Ocean* **1989**, *27*, 565–576. [[CrossRef](#)]
47. Coombes, C.A.; Harrison, A.W. Calibration of a three-component angular distribution model of sky radiance. *Atmos Ocean* **1988**, *26*, 183–192. [[CrossRef](#)]
48. Gregg, W.W.; Carder, K.L. A simple spectral solar irradiance model for cloudless maritime atmospheres. *Limnol. Ocean.* **1990**, *35*, 1657–1675. [[CrossRef](#)]
49. Volpe, G.; Dionisi, D.; Brando, V.; Colella, S.; Bracaglia, M.; Pitarch, J.; Falcini, F.; Sammartino, M.; Benincasa, M.; Santoleri, R. *IOPs Continuous Measurements for Ocean Monitoring and Calibration and Validation of Satellite Data*; EGU: Vienna, Austria, 2018; Volume 20, p. 16329.
50. Petzold, T.J. *Volume Scattering Functions for Selected Ocean Waters*; Scripps Institution of Oceanography: San Diego, CA, USA, 1972.
51. Maritorena, S.; Morel, A.; Gentili, B. Diffuse reflectance of oceanic shallow waters: Influence of water depth and bottom albedo. *Limnol. Ocean.* **1994**, *39*, 689–703. [[CrossRef](#)]
52. Simoncelli, S.; Fratianni, C.; Pinardi, N.; Grandi, A.; Drudi, M.; Oddo, P.; Dobricic, S.; Mediterranean Sea Physical Reanalysis (CMEMS MED-Physics) [Data Set]. Copernicus Monitoring Environment Marine Service (CMEMS). 2019. Available online: [https://doi.org/10.25423/MEDSEA\\_REANALYSIS\\_PHYS\\_006\\_004](https://doi.org/10.25423/MEDSEA_REANALYSIS_PHYS_006_004) (accessed on 28 February 2020).
53. Jouini, M.; Béranger, K.; Arsouze, T.; Beuvier, J.; Thiria, S.; Crépon, M.; Taupier-Letage, I. The sicily channel surface circulation revisited using a neural clustering analysis of a high-resolution simulation: The sicily channel surface circulation. *J. Geophys. Res. Ocean.* **2016**, *121*, 4545–4567. [[CrossRef](#)]
54. Copernicus Climate Change Service (C3S). ERA5: Fifth Generation of ECMWF Atmospheric Reanalyses of the Global Climate. Copernicus Climate Change Service Climate Data Store (CDS), June 2019. 2017. Available online: <https://cds.climate.copernicus.eu/cdsapp#!/home> (accessed on 28 February 2020).
55. Pace, G.; Cremona, G.; di Sarra, A.; Meloni, D.; Monteleone, F.; Sferlazzo, D.; Zaninin, G. Continuous vertical profiles of temperature and humidity at Lampedusa island. In Proceedings of the 9th International Symposium on Tropospheric Profiling, L'Aquila, Italy, 3–7 September 2012.
56. Kotsias, G.; Lolis, C.J. A study on the total cloud cover variability over the Mediterranean region during the period 1979–2014 with the use of the ERA-Interim database. *Theor. Appl. Climatol.* **2018**, *134*, 325–336. [[CrossRef](#)]
57. Meloni, D.; di Sarra, A.; Biavati, G.; DeLuisi, J.J.; Monteleone, F.; Pace, G.; Piacentino, S.; Sferlazzo, D.M. Seasonal behavior of Saharan dust events at the Mediterranean island of Lampedusa in the period 1999–2005. *Atmos. Environ.* **2007**, *41*, 3041–3056. [[CrossRef](#)]
58. Long, C.N.; Ackerman, T.P. Identification of clear skies from broadband pyranometer measurements and calculation of downwelling shortwave cloud effects. *J. Geophys. Res. Atmos.* **2000**, *105*, 15609–15626. [[CrossRef](#)]
59. Trisolino, P.; di Sarra, A.; Anello, F.; Bommarito, C.; Di Iorio, T.; Meloni, D.; Monteleone, F.; Pace, G.; Piacentino, S.; Sferlazzo, D. A long-term time series of global and diffuse photosynthetically active radiation in the Mediterranean: Interannual variability and cloud effects. *Atmos. Chem. Phys.* **2018**, *18*, 7985–8000. [[CrossRef](#)]
60. Min, Q.; Wang, T.; Long, C.N.; Duan, M. Estimating fractional sky cover from spectral measurements. *J. Geophys. Res.* **2008**, *113*, D20208. [[CrossRef](#)]
61. Pace, G.; di Sarra, A.; Meloni, D.; Piacentino, S.; Chamard, P. Aerosol optical properties at Lampedusa (Central Mediterranean). 1. Influence of transport and identification of different aerosol types. *Atmos. Chem. Phys.* **2006**, *6*, 697–713. [[CrossRef](#)]



62. Meloni, D.; di Sarra, A.; Pace, G.; Monteleone, F. Aerosol optical properties at Lampedusa (Central Mediterranean). 2. Determination of single scattering albedo at two wavelengths for different aerosol types. *Atmos. Chem. Phys.* **2006**, *6*, 715–727. [[CrossRef](#)]
63. di Sarra, A.; Sferlazzo, D.; Meloni, D.; Anello, F.; Bommarito, C.; Corradini, S.; De Silvestri, L.; Di Iorio, T.; Monteleone, F.; Pace, G.; et al. Empirical correction of multifilter rotating shadowband radiometer (MFRSR) aerosol optical depths for the aerosol forward scattering and development of a long-term integrated MFRSR-Cimel dataset at Lampedusa. *Appl. Opt.* **2015**, *54*, 2725. [[CrossRef](#)] [[PubMed](#)]
64. Calzolari, G.; Nava, S.; Lucarelli, F.; Chiari, M.; Giannoni, M.; Becagli, S.; Traversi, R.; Marconi, M.; Frosini, D.; Severi, M.; et al. Characterization of PM<sub>10</sub> sources in the central Mediterranean. *Atmos. Chem. Phys.* **2015**, *15*, 13939–13955. [[CrossRef](#)]
65. Bulgarelli, B.; Zibordi, G. Analysis of Adjacency Effects for Copernicus Ocean Colour Missions. 2018. Available online: <https://www.semanticscholar.org/paper/Analysis-of-adjacency-effects-for-Copernicus-Ocean-Barbara-Giuseppe/018cffaf395d3cf29f2254073bbc7b5f7b8c4c8e> (accessed on 2 April 2020).
66. BIPM; IEC; IFCC; ILAC; ISO; IUPAC; IUPAP; OMIL. *Evaluation of Measurement Data—Guide to the Expression of Uncertainty in Measurement*; GUM 1995 with minor corrections; JCGM: Saint-Cloud, France, 2008.
67. BIPM; IEC; IFCC; ILAC; ISO; IUPAC; IUPAP; OMIL. *Evaluation of Measurement Data—Supplement 2 to the “Guide to the Expression of Uncertainty in Measurement”—Extension to Any Number of Output Quantities*; JCGM: Saint-Cloud, France, 2011.
68. Brown, S.W.; Flora, S.J.; Feinholz, M.E.; Yarbrough, M.A.; Houlihan, T.; Peters, D.; Kim, Y.S.; Mueller, J.L.; Johnson, C.B.; Clark, D.K. The marine optical buoy (MOBY) radiometric calibration and uncertainty budget for ocean colour satellite sensor vicarious calibration. In Proceedings of the SPIE on Optics & Photonics, Sensors, Systems, and Next-Generation Satellites XI, Florence, Italy, 17 October 2007.
69. Zibordi, G.; Melin, F.; Berthon, J.-F. A regional assessment of OLCI data products. *IEEE Geosci. Remote Sens. Lett.* **2018**, *15*, 1490–1494. [[CrossRef](#)]
70. Franz, B.A.; Bailey, S.W.; Werdell, P.J.; McClain, C.R. Sensor-independent approach to the vicarious calibration of satellite ocean color radiometry. *Appl. Opt.* **2007**, *46*, 5068. [[CrossRef](#)]
71. Antoine, D.; Morel, A. A multiple scattering algorithm for atmospheric correction of remotely sensed ocean colour (MERIS instrument): Principle and implementation for atmospheres carrying various aerosols including absorbing ones. *Int. J. Remote Sens.* **1999**, *20*, 1875–1916. [[CrossRef](#)]
72. Voss, K.J.; Johnson, B.C.; Yarbrough, M.A.; Gleason, A. *Moby-Net: An Ocean Colour Vicarious Calibration System*; Earth Science Technology Forum: Pasadena, CA, USA, 2015.
73. Zibordi, G.; Holden, B.; Melin, F.; D’Alimonte, D.; Berthon, J.F.; Slutsker, I.; Giles, D. AERONET-OC: An overview. *Can. J. Remote Sens.* **2010**, *488*–497. [[CrossRef](#)]
74. Israelevich, P.; Ganor, E.; Alpert, P.; Kishcha, P.; Stupp, A. Predominant transport paths of Saharan dust over the Mediterranean Sea to Europe: Saharan dust transport to europe. *J. Geophys. Res. Atmos.* **2012**, *117*. [[CrossRef](#)]

